



**Arab American University
Faculty of Graduate Studies**

Tungsten doping effects on the properties of

$\text{Bi}_{1.5}\text{Zn}_{0.92}\text{Nb}_{1.5}\text{O}_{6.92}$ (BZN) ceramics

By

Mays Ahmad Abd Al Ghafoor

Supervisor:

Prof. Dr. Atef Qasrawi

This thesis was submitted in partial fulfillment of the
requirements for

**The Master's degree in Physics
February/2019**

© Arab American University 2019. All rights reserved.

Tungsten doping effects on the properties of
 $\text{Bi}_{1.5}\text{Zn}_{0.92}\text{Nb}_{1.5}\text{O}_{6.92}$ (BZN) ceramics

By

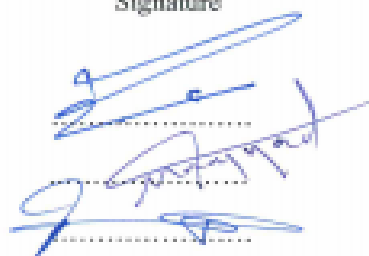
Mays Ahmad Abd Al Ghafoor

This thesis was defended successfully on 9.2.2019 and approved by:

Committee members

Signature

1. Prof. Dr. Atef Fayed Qasrawi (supervisor)
2. Dr. Muayad Abu- Saa (Internal Examiner)
3. Dr. Iyad Saadeeddin (External Examiner)



Declaration

The work provided in this thesis, unless otherwise referenced, is the researcher's own work and has not been submitted elsewhere for any other degree or qualification.

Student's Name:

Signature:

Date:

Dedication

To My Parents

Acknowledgments

I thank Almighty Allah for giving me the courage and the determination to do this thesis. I would be honor to dedicate this work to my lovely parents, who gave me the power and values necessary to be where I am standing today. Thanks for giving me the chance to improve myself. Thanks for all love and support. My lovely mother thanks you for all support steps per step in my life and study. Thanks for teaching me how to take my decision alone in order to learn from my personal mistakes, I always remember your special words "learn and grow from each seatback". Really, the word thanks do not enough to express my super mom. My father, thanks for all your love and work to give me a happy life, thank you for your trust, effort and proud. I promise you that I will stay like this in your eyes, your small special daughter. My family, sisters and brother's thanks for your kindness and extensive support, I hope to make you proud of your small sister the same way that I am proud of having you in my life. Special thanks to my brother Hussein for standing by my side from the beginning of the journey and supporting. My second family, whom I joined a short time, thanking them for their love and support. A great thanks to my life partner, to those who gathered me with the love of my life Wael, and also my son who has not come to life yet.

There are people in everyone's live who make success both possible and rewarding

My special thanks and heartfelt gratitude to Prof. Dr. Atef Qasrawi for his support and working hard with me to do this work. I hope to be like you one day. I learn from you how to be very good person in your life and work hard at yourself to achieve your dreams. Thanks because you made me believe that I have so much strength and courage to do this thesis (thanks best friend).

My genuine thanks to all department members: Prof. Dr. Zaki Saleh, Dr. Adli Saleh, Dr. Ahmad Omar, Prof. Mohammad Abu Samra, Dr. Soliman Rabaa, and Mr. Anan Hussien I wish to express my sincere thanks to internal examiner Dr. Moayd Abu Saa and external examiner Dr. Iyad Saadeddin for their support, valuable suggestions and critical comments.

I would to thank the research assistance Olfat Omareya for everything, she's a perfect friends and assistance and all my friends on a master's journey.

Abstract

In this thesis, the tungsten doping effects on the morphological, structural, compositional, electrical and optical properties of the bismuth zinc niobium oxide pyrochlore ceramics in accordance with the chemical formula $\text{Bi}_{1.5}\text{Zn}_{0.92}\text{Nb}_{1.5-6x/5}\text{W}_x\text{O}_{6.92}$ are investigated. The tungsten content is varied in the range of 0.10-0.18. While the structural properties were investigated by means of X-ray diffraction where a new minor phase has appeared indicating the solubility limit at $x = 0.18$, the morphology and energy dispersive X-ray analysis confirms this result. The temperature dependent XRD analysis was employed to determine the temperature effects on the lattice constant, grain size, micro strain, dislocation density and degree of orientation. In addition, the room temperature impedance spectra are recorded in the frequency range from 0.01 to 1.8 GHz. The physical parameters of capacitance, conductance, reflection coefficient, return loss and voltage standing wave ratio that are needed to show the ability of using the W-BZN as an active resonator in telecommunication technology were investigated. The effect of W content on the electrical resistivity is evaluated by dc measurements in the temperature range of 298-487 K. The activation energy is less than half of the energy band gap indicating the extrinsic nature of conduction. The energy band gap is found to be of direct allowed type.

Keywords: BZN; doping; tungsten; impedance spectroscopy; resistivity.

List of contents

Title		Page No.
List of Table		X
List of figure		XI
Chapter I	Introduction and Literature Survey	2
Chapter II	Theoretical Background	6
	2.1 Definition of pyrochlore	6
	2.2 X-ray diffraction	7
	2.2.1 Bragg's Law	7
	2.2.2 Investigation of lattice parameters from x-ray diffraction	9
	2.3 The modified Scherrer equation	13
	2.4 Identification of dislocation density	15
	2.5 Tauc's Relation	15
	2.6 RLC circuit	16
	2.7 Electrical conductivity by thermionic emission	18
	2.8 Voltage standing wave ratio	19
	2.9 The optical properties	19
Chapter III	Experimental Details	21
	3.1 Pyrochlore ceramics preparation	21
	3.2 Structural measurements	21

3.3	Impedance spectroscopy measurements	23
3.4	Current-Voltage measurements	24
3.5	Optical measurements	26
Chapter VI	Results and Discussion	27
4.1	Tungsten doping ratio effect on the structural properties	27
4.2	Temperature dependent XRD analysis for $\text{Bi}_{1.5}\text{Zn}_{0.92}\text{Nb}_{1.5}\text{W}_x\text{O}_{6.92}$	38
4.3	Scanning Electron microscopy and energy dispersive X-ray analysis	47
4.4	Impedance spectroscopy of W doped BZN	50
4.5	Electrical properties for $\text{Bi}_{1.5}\text{Zn}_{0.92}\text{Nb}_{1.5}\text{W}_x\text{O}_{6.92}$	58
4.6	Optical properties for $\text{Bi}_{1.5}\text{Zn}_{0.92}\text{Nb}_{1.5}\text{W}_x\text{O}_{6.92}$	61
Conclusions		67
References		69
Conferences		74
الملخص		75

List of tables

Table No.	Table Title	Page No.
4.1.1	The ionic radius of the BZN pyrochlore ceramics components.	28
4.1.2	2Θ , inter planer space and intensity for maximum peak as a function of W content for the BZN ceramics at room temperature (298 K).	30
4.1.3	The materials that can be formed inside W-BZN pyrochlore ceramics and direction	32
4.1.4	The mechanical parameters of the maximum peak as a function of W content for the BZN ceramics at room temperature (298 K)	34
4.5.1	The activation energy of W-BZN from $x=0.10$ to $x=0.18$	60

List of figures

Figure No.	Figure caption	Page No.
2.1	Bragg's condition	8
2.2	RLC series circuit	16
3.1	The diffraction of X-ray	22
3.2	The X-ray diffractometer	23
3.3	Agilent 4291B RF Signal Generator impedance analyzer	24
3.4	The current voltage device	25
3.5	The UV-VIS spectrophotometer	26
4.1.1	The 3-D X-ray diffraction patterns at $x = 0.10$ to $x = 0.18$ for $\text{Bi}_{1.5}\text{Zn}_{0.92}\text{Nb}_{1.5-6x/5}\text{W}_x\text{O}_{6.92}$ solid solutions at room temperature.	29
4.1.2	The X-ray diffraction patterns for BZN doped with W at digit rate angle of $2\theta = 30^\circ$ and at $2\theta = 59^\circ$.	31
4.1.3	The X-ray diffraction patterns at $x = 0.10$ and $x = 0.18$ for $\text{Bi}_{1.5}\text{Zn}_{0.92}\text{Nb}_{1.5-6x/5}\text{W}_x\text{O}_{6.92}$ solid solutions at room temperature.	33
4.1.4	(a) crystallite size (b) Strain (c) Dislocation density (d) degree of orientation (K) for W doped BZN pyrochlore ceramics.	36
4.1.5	Variation of the lattice constant with W content	37
4.2.1	The X-ray diffraction patterns at $x = 0.17$ for $\text{Bi}_{1.5}\text{Zn}_{0.92}\text{Nb}_{1.5-6x/5}\text{W}_x\text{O}_{6.92}$ solid solutions at $2\theta = 30.2^\circ$ and at $2\theta = 49.7^\circ$ as a function of temperature.	38
4.2.2	(a) crystallite size (b) Strain (c) Dislocation density of W-BZN as a function of temperature for $x = 0.17$.	40
4.2.3	The X-ray diffraction patterns for $\text{Bi}_{1.5}\text{Zn}_{0.92}\text{Nb}_{1.5-6x/5}\text{W}_x\text{O}_{6.92}$ with $x = 0.18$ as a function of temperature.	41

4.2.4	The X-ray diffraction patterns at $x=0.18$ for $\text{Bi}_{1.5}\text{Zn}_{0.92}\text{Nb}_{1.5-6x/5}\text{W}_x\text{O}_{6.92}$ solid solutions at $2\theta=30.4^\circ$ as a function of temperature.	43
4.2.5	The X-ray diffraction patterns at $x=0.18$ for $\text{Bi}_{1.5}\text{Zn}_{0.92}\text{Nb}_{1.5-6x/5}\text{W}_x\text{O}_{6.92}$ solid solutions at $2\theta=30.4^\circ$ as a function of temperature of before and after heating.	44
4.2.6	(a) crystallite size (b) Strain (c) Dislocation density (d) degree of orientation of W-BZN as a function of temperature for $x=0.18$.	46
4.3.1	The scanning electron microscopy images for the $\text{Bi}_{1.5}\text{Zn}_{0.92}\text{Nb}_{1.5-6x/5}\text{W}_x\text{O}_{6.92}$ pyrochlore composition of ($x=0.17$) being enlarged 15000 times.	48
4.3.2	The scanning electron microscopy images for $\text{Bi}_{1.5}\text{Zn}_{0.92}\text{Nb}_{1.5-6x/5}\text{W}_x\text{O}_{6.92}$ pyrochlore ceramics doped with tungsten of content of $x=0.18$ (a) enlargement of 2.000 times b) enlargement of 5000 times, c) point 1 EDS analysis showing that the W-doped BZN exceeds the solubility limit with the presence of Bi_2WO_6 and d) point 2 the EDS analysis showing the pyrochlore itself.	49
4.4.1	The capacitance spectra for $\text{Bi}_{1.5}\text{Zn}_{0.92}\text{Nb}_{1.5-6x/5}\text{W}_x\text{O}_{6.92}$ pyrochlore ceramics being registred at room temperature.	51
4.4.2	The conductance of W-BZN as a function of frequency.	52
4.4.3	The impedance of W-BZN as a function of frequency.	54
4.4.4	The reflection coefficient of W-BZN as a function of frequency.	55
4.4.5	The return loss of W-BZN as a function of frequency.	56
4.4.6	The VSWR of W-BZN as a function of frequency.	57
4.5.1	Variation of electrical resistivity of the W_BZN with temperature.	59
4.5.2	The $\ln(\rho)-1000/T^{-1}$ dependence.	60
4.6.1	The transmittance of $\text{Bi}_{1.5}\text{Zn}_{0.92}\text{Nb}_{1.5-6x/5}\text{W}_x\text{O}_{6.92}$ solid solutions.	61
4.6.2	Reflectance of $\text{Bi}_{1.5}\text{Zn}_{0.92}\text{Nb}_{1.5-6x/5}\text{W}_x\text{O}_{6.92}$ solid solutions.	62
4.6.3	Absorption coefficient of $\text{Bi}_{1.5}\text{Zn}_{0.92}\text{Nb}_{1.5-6x/5}\text{W}_x\text{O}_{6.92}$ solid solutions.	64
4.6.4	$(\alpha E)^2$ versus E for W doped BZN pyrochlore ceramics.	65

List of symbols

Symbol	
x	The content of doping in the sample
ϵ_r	Dielectric constant
$\tan\delta$	Dielectric loss tangent
τ_ϵ	Temperature coefficient of the dielectric constant
ppm	Parts per million
Q_f	Quality factor
Fd-3m	Cubic crystal system
λ	Wavelength
Θ	Incident angle
d	The interplanar spacing of crystal planes
n	Positive integer
hkl	Miller index
a, b, c	The lengths of the cell edges
α, β, γ	The angle between the cell edges
D	Crystallite size
K	The shape factor
B	Peak broadenings
m	Integer
t	Thickness of crystal
δ	Dislocation density
ϵ	Strain
a	Lattice constant
E_g	Energy gap
E	Photon energy
α	Absorption coefficient
A	Constant
P	Constant related to the optical transition
R	Resistance
C	Capacitance
L	Inductance
Z	Impedance
X	Reactive
X_L	Inductive reactance
X_C	Capacitive reactance
F	Frequency
ϵ_0	Permittivity of free space
VSWR	Voltage standing wave ratio
ρ	Reflection coefficient
K	Degree of orientation
EDS	The energy dispersive X-ray analyzer

G	Conductance
Ω	Ohm
Lr	Return loss
dB	Decibel unit
ρ	Electrical resistivity
E _a	Activation energy

List of acroname

Role No.	Role name
2.1	Bragg's law
2.2	The Strain relation
2.3	The Degree of orientation relation
2.4	The Triclinic relation
2.8	The Monoclinic relation
2.10	The Orthorhombic relation
2.12	The Rhombohedral relation
2.15	The Hexagonal relation
2.17	The Tetragonal relation
2.19	The Cubic relation
2.20	The Scherrer equation
2.28	The Dislocation density relation
2.29	The Tauc's relation
2.30	The Impedance relation
2.36	The Electric conductivity relation
2.37	The Voltage Standing Wave Ratio relation
4.1	The Transmittance relation

Chapter One

Introduction and Literature survey

Ceramic materials have many featured characteristics such as low density, high mechanical strength, high wear resistance, low thermal expansion, high or low thermal conductivity, which make it attractive for industry. One of the ceramic groups that attracted the attention is the pyrochlore ceramics famously presented by bismuth zinc niobium oxide (BZN).

The BZN pyrochlore ceramics are used to produce capacitors and dielectric resonators. It exhibits excellent microwave dielectric properties [1]. The BZN pyrochlore ceramics is also employed for optical applications in the visible region of light such as photovoltaic devices. The pyrochlore ceramics can perform as passive mode operation devices like microwave capacitors because of the remarkable increase in the dielectric constant in response to signal frequency [2]. In addition, BZN has negative dielectric property (Inability of the material to resist the electric field, the dielectric function can be negative but only over certain specific regions of frequency) that is useful in applications where the cancelation of parasitic capacitance is needed [3]. Moreover, the BZN pyrochlore ceramics is characterized by response time, required level of tunability, operating temperature, and loss tangent which make it good material in many applications as phase shifters, antenna beam steering, filters, voltage controlled oscillators, matching networks, and tunable power splitters [4].

BZN pyrochlore ceramics are prepared by two-step sintering method which is used to prepare complex perovskite BZN pyrochlore ceramics. The sintering aims to inhibit the

“order-disorder” transitions before densing. This technique lowered the sintering temperature to less temperature than the transition temperature making it better than conventional sintering processes [5]. The BZN ceramics prepared by two-step sintering processes exhibit a high degree of cation ordering. Another way to prepare the BZN ceramics is the solid state reaction method. In this method, Bi_2O_3 , ZnO and Nb_2O_3 were mixed with Lanthanum (La) in ethanol for 15 hrs. The sample was then dried at $100\text{ }^\circ\text{C}$ for one day, after that it was calcinated for 4 hrs at $800\text{ }^\circ\text{C}$. After the powder of BZN was produced, a pellet of BZN was pressed at pressure of 2 MPa, and sintered at temperature of $900\text{ }^\circ\text{C}$ – $1100\text{ }^\circ\text{C}$ for 4 hrs [6].

Several types of techniques have been employed to reflect the characteristics of the BZN pyrochlore ceramics including the electrical, optical and dielectric properties. One of these techniques is the doping of the bismuth zinc niobium oxide ceramics. By the conventional solid-state reaction method, the BZN pyrochlore ceramic doped with Ca^{+2} was prepared in A-site and B-site. The effects of Ca^{+2} on the structure and dielectric properties on the dielectric relaxation degree of BZN ceramics were discovered [7]. The BZN ceramics shown excellent relative dielectric properties of dielectric constant ($\epsilon_r = 132$), dielectric loss tangent ($\tan\delta = 2.45 \times 10^{-3}$) and temperature coefficient of the dielectric constant ($\tau_\epsilon = -17\text{ ppm}/^\circ\text{C}$) with the low-firing temperature of $950\text{ }^\circ\text{C}$, when doped with Mn [8]. In another work, introduction of the CuO into BZN ceramics by modifying the surface of BZN with a CuO thin layer on the calcined powder instead of mixing CuO directly with BZN powder lowered the densification temperature to $900\text{ }^\circ\text{C}$. The BZN ceramics which are sintered at $900\text{ }^\circ\text{C}$ presented good microwave dielectric properties presented by $\epsilon_r =$

141 and quality factor ($Qf = 426$ GHz) [9]. On the other hand, Laser pulsed deposition technique which is used to dope bismuth zinc niobate thin films with calcium exhibits a dielectric constant and loss tangent values of 67.2 and 0.03 at 100 kHz, respectively [10]. Increasing the yttrium doping content from 0.04 to 0.07 in the BZN decreases the optical energy band gap from 3.60 to 2.75 eVs [11]. Also, nickel doping affected the optical and electrical properties of BZN pyrochlore ceramics and altered the energy gap from 3.30 eV to 3.52 eV. The temperature dependent electrical resistivity also increased with increasing Ni content from 0.00 to 0.10 [12]. The indium and iridium doping into BZN pyrochlore altered the relative permittivity of the BZN ceramics. Namely, the relative permittivity of Ir doped BZN slightly decreased with Ir content. However, n doping into the BZN decreased the relative permittivity at low doping ratios, but increased it at high doping ratios [13]. The hafnium (Hf) doping effects on the optical, structural, compositional, electrical and dielectric properties of the BZN ceramics are also investigated. Increasing the Hf content from 0.03 to 0.06 decreased the room temperature, strain, dislocation density, lattice constant and electrical resistivity. Also, the dielectric constant and the crystallite size were increased. In addition, when the Hf contents is increased from 0.03 to 0.06, the energy bands gap decreased from 3.30 to 2.21 and reached 2.10 eV, respectively [2].

In this thesis, the target is to insert another doping type to the BZN. The effects of tungsten doping from optical, electrical, structural, compositional and dielectric point of view of the BZN pyrochlore ceramics will be considered. Particularly, we aim to explore the changes that are related to the doping of W into the Nb sites of the BZN pyrochlore ceramics. In second chapter of this thesis, the theoretical background needed for analyzing

the observed experimental results are reported. Particularly, notes of the X-ray diffraction technique, optical absorption, and method of band gap estimation are reported. In addition, the resistance, inductance, capacitance circuit analyses are reported to clarify the microwave signals. In third chapter, the experimental details and mechanisms needed for explaining the techniques are reported. In fourth chapter, the results obtained during the experiments were explained and discussed. Finally, the concluding remarks are reported and discussed.

Chapter Two

Theoretical Background

2.1. Definition of pyrochlore

The pyrochlore (more comprehensive term for the pyrochlore crystal structure (Fd-3m)) is a mineral group of the niobium end member of the pyrochlore supergroup. The more general crystal structure describes materials of the type $A_2B_2O_6$ and $A_2B_2O_7$ where the A and B species are generally transition metal species or rare-earth [14, 15].

The pyrochlore structure is a super structure derivative of the simple fluorite structure ($AO_2 = A_4O_8$, where the A and B cations are ordered along the $\langle 110 \rangle$ direction. The additional anion vacancy resides in the tetrahedral interstice between adjacent B-site cations. These systems are particularly susceptible to geometrical frustration and novel magnetic effects.

The pyrochlores are important for diverse technological applications:

1. Luminescence.
2. Ionic conductivity.
3. Nuclear waste immobilization.
4. High temperature thermal barrier coatings.
5. Automobile exhaust gas control.
6. Catalysts.
7. Solid oxide fuel cell.
8. Ionic/electric conductors.

2.2. X-ray diffraction technique

X-rays are high-energy electromagnetic radiation. They have energies ranging from about 200 eV to 1 MeV, which puts them between γ -rays and ultraviolet (UV) radiation in the electromagnetic spectrum [16].

The X-ray diffraction (XRD) is an effective tool to investigate the structural properties of materials. One may be able to define the atomic spacing, plane orientation and lattice parameters from this technique. In addition, it is possible to determine the lattice deformation by this technique.

2.2.1. Bragg's Law

Bragg gave a simple interpretation of the XRD diffraction pattern, according to Bragg, the diffraction spots produced are due to the reflection of some of the incident X-rays by various sets of parallel crystal planes. These planes are called Bragg's planes. The Bragg's interpretation is explained in the following paragraph.

Considering the XRD as the process of reflection of X-ray by crystal planes as shown in Fig.2.1. A monochromatic X-ray beam of wavelength λ is incident at an angle θ to a family of Bragg planes. Assuming the interplanar spacing of crystal planes "d", as shown in the figure. The dots in the planes represent positions of atoms in the crystal. Every atom in the crystal is a source of scattered X-rays [17], thus,

$$2d\sin\theta = n\lambda \quad (2.1)$$

Where, n is a positive integer

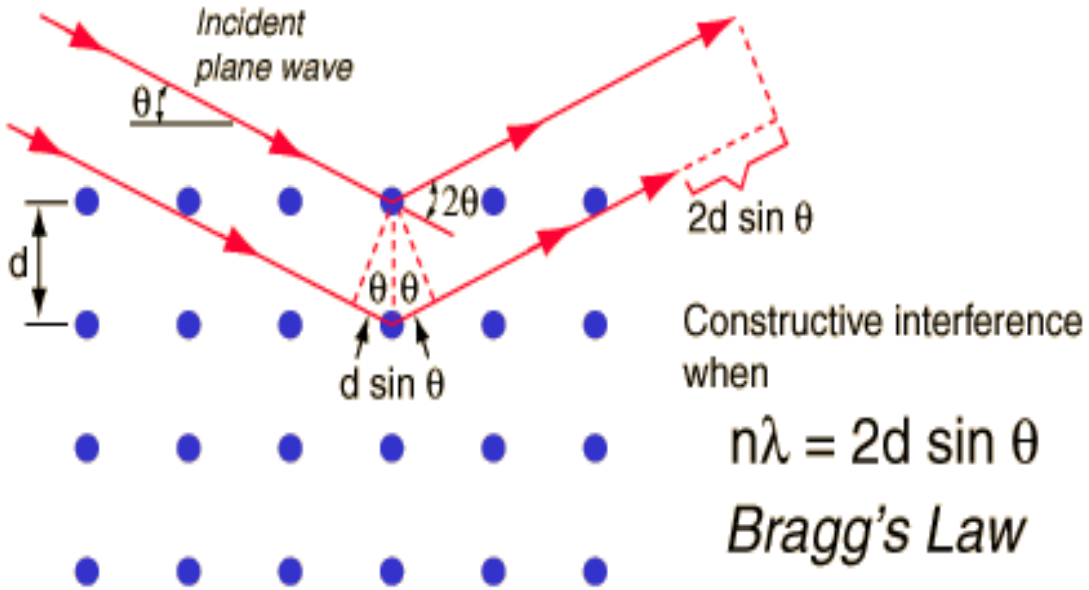


Fig.2.1: Bragg's condition [18]

The strain is the ratio between the changes in the bond length to the original bond length which may be calculated from strain equation [19]

$$\varepsilon = \frac{0.94\lambda}{\tan\theta} \quad (2.2)$$

Where (ε) is the strain, (λ), (D) is the grain size and (θ) is incident angle.

The degree of orientation is the Polymers are never 100% crystalline which is calculated using both the intensity of the maximum peak and the summation of the intensities of all observed diffraction peaks

$$k = \frac{I_{max}}{\sum I} \quad (2.3)$$

2.2.2. Investigation of lattice parameters from X-ray diffraction

The point symmetry groups in 3-D require the seven types of cell crystal system, which are triclinic, monoclinic, orthorhombic, tetragonal, cubic, trigonal, and hexagonal. These are divided into 14 different lattice types called bravais lattices. The general lattice is triclinic, and there are 13 special lattices. The spacing (d) between adjacent (hkl) lattice planes of the triclinic system is given by:

$$\frac{1}{d^2} = \frac{\frac{h^2}{a^2} \sin^2 \alpha + \frac{k^2}{b^2} \sin^2 \beta + \frac{l^2}{c^2} \sin^2 \gamma + \frac{2kl}{bc} \cos \alpha + \frac{2hl}{ac} \cos \beta + \frac{2hk}{ab} \cos \gamma}{1 - \cos^2 \alpha - \cos^2 \beta - \cos^2 \gamma + 2 \cos \alpha \cos \beta \cos \gamma} \quad (2.4)$$

Where,

a, b and c are the lattice constant

α , β and γ are the angles between the lattice.

h, k and l are miller indices

The spacing relations of monoclinic, orthorhombic, tetragonal, cubic, trigonal, and hexagonal can be derived from the triclinic equation by substituting the systems lattice parameters as follows:

1. Monoclinic relation:

substitute

$$a \neq b \neq c, \alpha = \gamma = 90, \beta \neq 90$$

so,

$$\cos \alpha = \cos \gamma = 0, \sin \alpha = \sin \gamma = 1, \text{ hance}$$

$$\frac{1}{d^2} = \frac{\frac{h^2}{a^2}1^2 + \frac{k^2}{b^2}\sin^2 \beta + \frac{l^2}{c^2}1^2 + \frac{2kl}{bc}(0) + \frac{2hl}{ac}\cos \beta + \frac{2hk}{ab}(0)}{1 - 0^2 - \cos^2 \beta - 0^2 + 2(0)\cos \beta(0)} \quad (2.5)$$

$$= \frac{\frac{h^2}{a^2} + \frac{l^2}{c^2} + \frac{k^2}{b^2}\sin^2 \beta + \frac{2hl}{ac}\cos \beta}{1 - \cos^2 \beta} \quad (2.6)$$

But

$$\frac{1}{1 - \cos^2 \theta} = \csc^2 \theta, \text{ relation (2.3) can be written as} \quad (2.7)$$

$$\frac{1}{d^2} = \left(\frac{h^2}{a^2} + \frac{k^2}{b^2}\sin^2 \beta + \frac{l^2}{c^2} - \frac{2hl}{ac}\cos \beta \right) \csc^2 \beta \quad (2.8)$$

Orthorhombic relation:

The lattice parameters are

$$a \neq b \neq c, \alpha = \beta = \gamma = 90$$

so,

$$\cos \alpha = \cos \beta = \cos \gamma = 0, \sin \alpha = \sin \beta = \sin \gamma = 1$$

then spacing d can be deduced as follows

$$\frac{1}{d^2} = \frac{\frac{h^2}{a^2}1^2 + \frac{k^2}{b^2}1^2 + \frac{l^2}{c^2}1^2 + \frac{2kl}{bc}(0) + \frac{2hl}{ac}(0) + \frac{2hk}{ab}(0)}{1 - 0^2 - 0^2 - 0^2 + 2(0)} \quad (2.9)$$

Which is simplified to

$$\frac{1}{d^2} = \frac{h^2}{a^2} + \frac{k^2}{b^2} + \frac{l^2}{c^2} \quad (2.10)$$

Rhombohedral relation:

With lattice parameters

$$a = b = c, \alpha = \beta = \gamma \neq 90$$

the spacing d can be written as

$$\frac{1}{d^2} = \frac{\frac{h^2}{a^2} \sin^2 \alpha + \frac{k^2}{b^2} \sin^2 \alpha + \frac{l^2}{c^2} \sin^2 \alpha + \frac{2kl}{bc} \cos \alpha + \frac{2hl}{ac} \cos \alpha + \frac{2hk}{ab} \cos \alpha}{1 - \cos^2 \alpha - \cos^2 \alpha - \cos^2 \alpha + 2 \cos \alpha \cos \alpha \cos \alpha} \quad (2.11)$$

Which is reduced to

$$\frac{1}{d^2} = \frac{(h^2 + k^2 + l^2) \sin^2 \alpha + 2(hk + kl + hl)(\cos^2 \alpha - \cos \alpha)}{a^2(1 - 3 \cos^2 \alpha + 2 \cos^3 \alpha)} \quad (2.12)$$

Hexagonal relation:

Substitute the following parameters in relation (2.4)

$$a = b \neq c, \alpha = \beta = 90, \gamma = 120$$

so

$$\cos \alpha = \cos \beta = 0, \cos \gamma = -0.5, \sin \alpha = \sin \beta = 1, \sin \gamma = 0.8$$

the spacing d becomes

$$\frac{1}{d^2} = \frac{\frac{h^2}{a^2} 1^2 + \frac{k^2}{a^2} 1^2 + \frac{l^2}{c^2} 0.8^2 + \frac{2kl}{ac} (0) + \frac{2hl}{ac} (0) + \frac{2hk}{a^2} (-0.5)}{1 - 0 - 0 + 0.5 + 0} \quad (2.13)$$

This is reduced to

$$\frac{1}{d^2} = \frac{\frac{h^2}{a^2} + \frac{k^2}{a^2} + \frac{l^2}{c^2} 0.8^2 + \frac{2hk}{a^2}(-0.5)}{0.75} \quad (2.14)$$

and finally can be written as

$$\frac{1}{d^2} = \frac{4}{3} \left(\frac{h^2 + k^2 + hk}{a^2} \right) + \frac{l^2}{c^2} \quad (2.15)$$

Tetragonal relation:

The parameters are

$$a = b \neq c, \alpha = \beta = \gamma = 90$$

hance

$$\cos\alpha = \cos\beta = \cos\gamma = 0, \sin\alpha = \sin\beta = \sin\gamma = 1$$

this gives

$$\frac{1}{d^2} = \frac{\frac{h^2}{a^2} 1^2 + \frac{k^2}{a^2} 1^2 + \frac{l^2}{c^2} 1^2 + \frac{2kl}{ac}(0) + \frac{2hl}{ac}(0) + \frac{2hk}{a^2}(0)}{1 - 0^2 - 0^2 - 0^2 + 2(0)} \quad (2.16)$$

Finally reduced to

$$\frac{1}{d^2} = \frac{h^2 + k^2}{a^2} + \frac{l^2}{c^2} \quad (2.17)$$

Cubic relation:

With its simplest lattice parameters

$$a = b = c, \alpha = \beta = \gamma = 90$$

these gives

$$\cos\alpha = \cos\beta = \cos\gamma = 0, \sin\alpha = \sin\beta = \sin\gamma = 1$$

and lattice spacing relation becomes

$$\frac{1}{d^2} = \frac{\frac{h^2}{a^2}1^2 + \frac{k^2}{a^2}1^2 + \frac{l^2}{a^2}1^2 + \frac{2kl}{a^2}(0) + \frac{2hl}{a^2}(0) + \frac{2hk}{a^2}(0)}{1 - 0^2 - 0^2 - 0^2 + 2(0)} \quad (2.18)$$

This gives simplest lattice spacing form

$$\frac{1}{d^2} = \frac{h^2 + k^2 + l^2}{a^2} \quad (2.19)$$

2.3. The modified Scherrer equation

Scherrer equation is one of many methods used to determine the grain size (D). The Scherrer equation was developed in 1918; it relates the grain size to the broadening of a diffraction peak.

The scherrer equation is given as:

$$D = \frac{K\lambda}{\beta \cos \theta} \quad (2.20)$$

Where, the constant K is the shape factor which related to crystallite shape and normally taken 0.94 $\lambda=1.5418$ °A is the Cu- α X-ray wavelength, β is the peak broadenings at full width half maximum peak in radians, and θ is Bragg's angle. The simplest way to derive the scherrer equation is the differentiation of Bragg's law, starting with multiplying both side of equation (2.1) by an integer m , and let $n=1$, then equation (2.1) becomes [20]:

$$m\lambda = 2md \sin \theta \quad (2.21)$$

Since that the interplanar distance d multiplied with m integers equal the thickness of crystal (t), then equation (2.21) simplifies as:

$$m\lambda = 2t\sin\theta \quad (2.22)$$

This equation can also be interpreted as the m^{th} order reflection from a set of planes with an interplanar distance (t). By differencing both side of equation (2.22) and noticing that $m\lambda$ is constant, this yields to:

$$0 = 2\Delta t \sin\theta + 2t \cos\theta \Delta\theta \quad (2.23)$$

$$t = \frac{\Delta t \sin\theta}{\Delta\theta \cos\theta} \quad (2.24)$$

Since the small increment in the thickness Δt is d , $d \sin(\Theta) = \lambda/2$ from equation (2.1), and $\Delta\Theta$ from given Θ can be positive or negative, so the absolute value must be taken. Hence, $\Delta\Theta$ is the half width of the peak and ($2\Delta\Theta = \beta$) is the full width half maximum peak. Substitution of these factors in equation (2.24) gives:

$$t = \frac{d \sin\theta}{\Delta\theta \cos\theta} = \frac{\lambda}{2\Delta\theta \cos\theta} \quad (2.25)$$

This is reduced to

$$t = D = \frac{\lambda}{\beta \cos\theta} \quad (2.26)$$

If the Gaussian function is used to describe the peak, a shape factor $K = 0.94$ is applied. Then Scherrer equation will be:

$$D = \frac{0.94\lambda}{\beta \cos\theta} \quad (2.27)$$

Where D is the grain size of the crystallites, β is the full width at half maximum intensity of peaks in radians; θ is Bragg's angle (in degrees). K is a constant related to the crystal shape, taken as 0.94. This equation has limitation presented by the crystallite size value which indicates the validity of the equation below 200 nm only.

2. 4. Identification of dislocation density

Dislocation density is defined as the total length of dislocation lines in a unit volume and in terms of unit and it is expressed as line/cm². The dislocation density is also expressed as number of lines per square metre, lines/m² calculated by using the following equation [21].

$$\delta = \frac{15\varepsilon}{aD} \quad (\text{line/cm}^2) \quad (2.28)$$

Where ε is the strain, a is the lattice constant and D is the grain size. Equation (2.28) implies that the strain increases, the dislocation density increases, indicating a crystallite with small strength. A material is very strong when the density of dislocations is negligibly small.

2.5. Tauc's Relation

In the absorption process, an electron in the valance band absorbs photon energy and excites to the conduction band leaving a hole in the valance band and an electron-hole pair is formed. The minimum value of energy required to generate an electron-hole pair called the band gap energy

E_g. The absorption coefficient α is employed to determine the energy gap E_g of the semiconductor using Tauc's relation:

$$(\alpha E)^{\frac{1}{p}} = A(E - E_g) \quad (2.29)$$

where α is the absorption coefficient, $E = h\nu$ is the photon energy, A is a constant determined by transition probability and related to the material properties, E_g is the energy band gap between valance and conduction band, and p is a constant related to the optical transition type. The values of p are 3/2, 3, 1/2 or 2 for forbidden direct, forbidden indirect, allowed direct and allowed indirect optical transitions, respectively. From the plot of $(\alpha E)^{1/p}$ versus the photon energy, the value of the energy band gap can be estimated by the intercept with E-axis for the best linear curve of $(\alpha E)^{2/3}$, $(\alpha E)^{1/3}$, $(\alpha E)^2$ and $(\alpha E)^{1/2}$, which includes the widest amount of data [22].

2.6. RLC circuit

AC circuits with resistors R , capacitors C , and inductors L are known as RLC circuits connected in series as shown in Fig.2.2. Since inductive reactance and capacitive reactance have opposite effects on the circuit phase angle, the total reactance is less than either individual reactance.

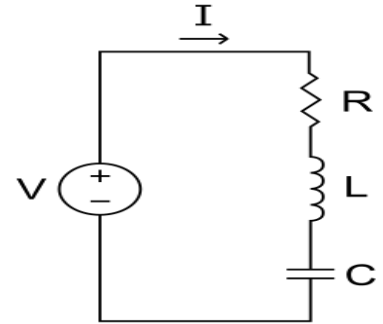


Fig.2.2: RLC series circuit

The capacitance, inductive reactance, and resistance in the circuit determine the total impedance. Total impedance affects the current in a circuit and the voltage across the components in the circuit.

$$|Z| = \sqrt{R^2 + X^2} \quad (2.30)$$

Where (Z) is the impedance, (R) is the resistance and (X) is the reactive component of Z.

The inductive reactance (X_L) causes the total current to lag the source voltage. Capacitive reactance (X_C) has the opposite effect: It causes the current to lead the voltage. Thus, X_L and X_C tend to offset each other. When they are equal, they cancel, and the total reactance is zero. In any case, the total reactance in a series circuit is

$$X_{tot} = |X_L - X_C| \quad (2.31)$$

$$X = \left| \frac{1}{2\pi f C} - 2\pi f L \right| \quad (2.32)$$

Where (C) is the capacitance, (L) is the inductance and (f) is the frequency.

RLC circuits follow the rules of all series and parallel circuits. In series circuits, the largest impedance has the greatest effect on the current in the circuit. In parallel circuits, the smallest impedance has the greatest effect on the current in the circuit.

The admittance is a measure of how easily a circuit or device will allow a current to flow [23].

$$Y = G + i B \quad (2.33)$$

Where (B) is the imaginary part (capacitive susceptance is the reciprocal of capacitive reactance and is a measure of the ability of a capacitor to permit current) and (G) is the real part, which represent the conductivity that we can calculate from following equation

$$G = \frac{R}{R^2 + X^2} \quad (2.34)$$

The dielectric constant $K\epsilon_0$ is the ability of the material to store the electrical energy in an electric field. It can be calculated from the following equation,

$$C = K \frac{\epsilon_0 A}{d} \quad (2.35)$$

Where (C) is the capacitance, (K) is the dielectric constant, (A) is the area of the sample, (d) is the distance between two electrodes and (ϵ_0) is the permittivity of free space.

2.7. Electrical conduction by thermionic emission:

Electric conductivity is one of the most delicate physical properties to characterize in insulating material. Electrical conductivity measurements in dielectric materials is carried out as a function of temperature. The electric conductivity as a function of temperature can be calculated from Arrhenius equation as follow [24].

$$\sigma = \sigma_0 e^{-E_a/KT} \quad (2.36)$$

Where (σ_0) is the preexponential factor, (k) is the Boltzman constant, (T) is the temperature and E_a is the activation energy.

Activation energy is the minimum amount of energy that is required to activate atoms or molecules to a condition in which they can undergo chemical transformation or physical transport. In transition-state theory, the activation energy is the difference in energy content between atoms or molecules in an activated or transition-state configuration and the corresponding atoms and molecules in their initial configuration. Activation energies are

determined from experimental rate constants or diffusion coefficients that are measured at different temperatures.

2.8. Voltage standing wave ratio (VSWR)

Voltage standing wave ratio (VSWR) is the ratio of the maximum to the minimum voltages in the line. During measurements, the probe was slid along the line through a distance of at least a quarter-wavelength to record the maximum and minimum voltages of the standing wave pattern. The maximum was proportional to $(1+\rho)$ and the minimum was proportional to $(1-\rho)$ [25]. VSWR is related to the magnitude of the voltage reflection coefficient ($|\Gamma|=\rho$) by:

$$VSWR = \frac{V_{max}}{V_{min}} = \frac{1 + |\Gamma|}{1 - |\Gamma|} = \frac{1 + \rho}{1 - \rho} \quad (2.37)$$

2.9. The optical properties

When a beam of light strikes a sample of thickness d , it is reflected by R of its original intensity I_0 . It also maintains $(1-R)$ of its original intensity when entering the sample. After that, a portion of the beam that enters the material propagates through the sample has an absorbed intensity multiplied by a factor $(e^{-\alpha d})$. The absorption coefficient can be used to visualize the energy band gap of semiconductors in which the Tauc relation (2.29) [26]:

Tuac plots $(\alpha E)^{1/p}$ -E give the E_g from the intercept on the E-axis in the linear region of the absorption onset with the baseline.

Chapter Three

Experimental Details

3.1 Pyrochlore ceramics preparation:

Our pyrochlore ceramics were prepared by the group in Marmara University, which were prepared by the solid-state reaction method at high temperatures. The following substances, Bi_2O_3 (99.99%), ZnO (99.5%) and Nb_2O_5 (99%) were mixed with tungsten oxide (WO_3) by ball milling for 15 h in ethanol. The pyrochlore ceramic was then dried at 100 °C for one day, after that it was calcinated for 4 hrs at 800 °C. After the powder of BZN was produced, a pellet of BZN was pressed at pressure of 2 MPa into disks, and composition the ceramics at temperature 900–1100 °C for 4 hrs. By this method, W- BZN pyrochlore ceramic with the stoichiometry formula was produced.

3.2 Structural measurements:

The XRD is a very important technique used to identify the structure of materials. The crystalline nature of the pyrochlore ceramics was identified by the Rigakua diffractometer equipped with K radiation of a copper anode of wavelength 1.5405 Å at 15 mA and 40 kV. The system of X-ray source consists of slit, detector, monochromator, filter and sample holder. Fig.3.1 shows the schematic of an XRD system. To obtain high resolution of the XRD, a 0.1 mm slit was used in the XRD system. We studied the effect of doping ratio of tungsten on the

structure of BZN by taking XRD for all samples with $x = 0.10, 0.15, 0.17$ and 0.18 at room temperature and lattice parameters were refined by the least square method. The temperature effect on the structure of the samples doped with tungsten of the content for $x = 0.18$ and $x = 0.17$ were studied in the range from $T = 298$ to $T = 473$ K by increasing 25 degrees for each measurement. The data were collected in the 2θ range of $10-70^\circ$. The obtained XRD data were analyzed using TREOR-92 evaluation computer program.

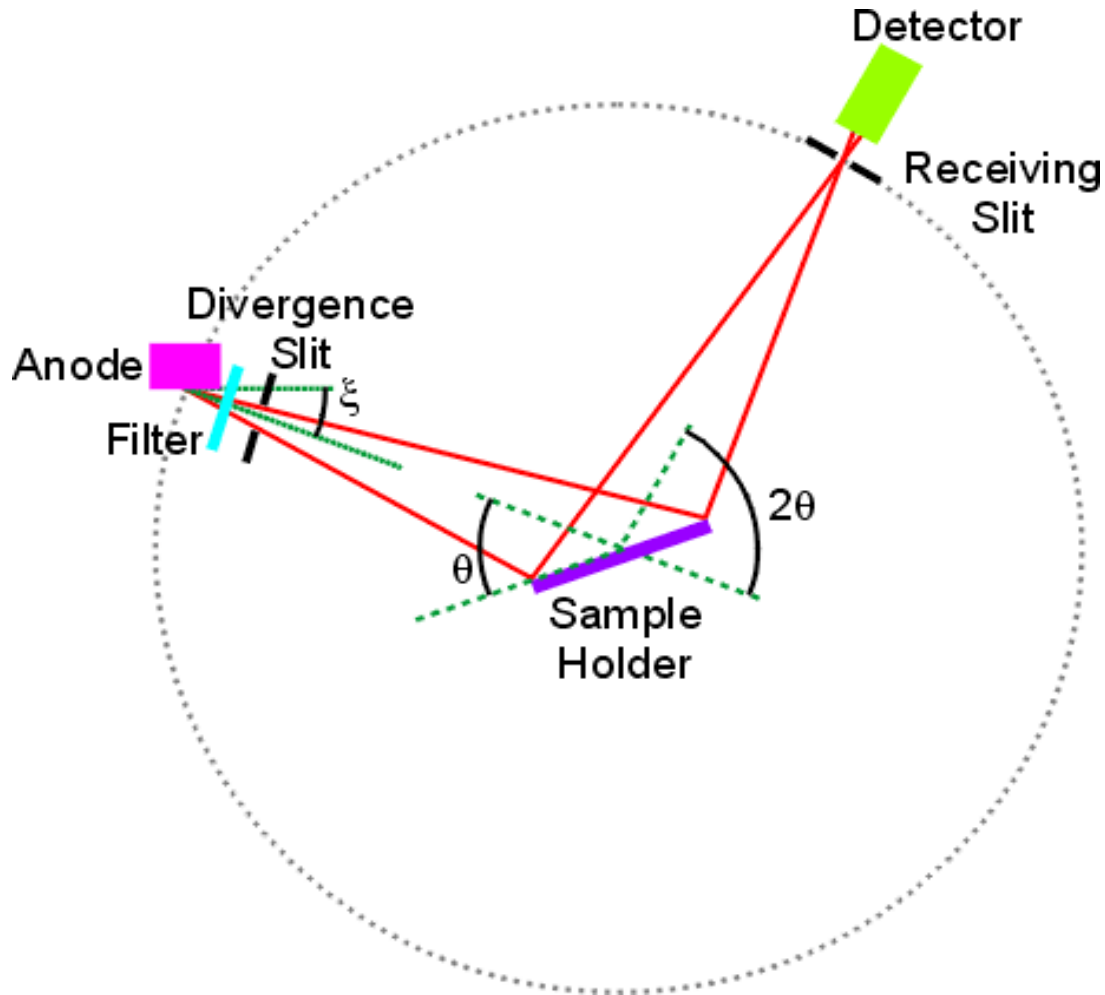


Fig. 3.1: The diffraction of X- ray [27].



Fig.3.2: The X-ray diffractometer

3.3: Impedance Spectroscopy measurements:

The impedance spectroscopy was measured by using Agilent 4291B RF 10–1.8GHz impedance analyzer to provide the Ac signal. The system is shown in Fig.3.3. The device determines the impedance (Z) that was composed of reactive and resistive parts. The reactive part is gained through the measurement of the capacitance (C) and inductance (L). On the other hand, the resistance is also measured. The signal power was recorded with the help of MATLAB

software. Remarkable characterization by measurements of output curves was performed with impedance spectroscopy.

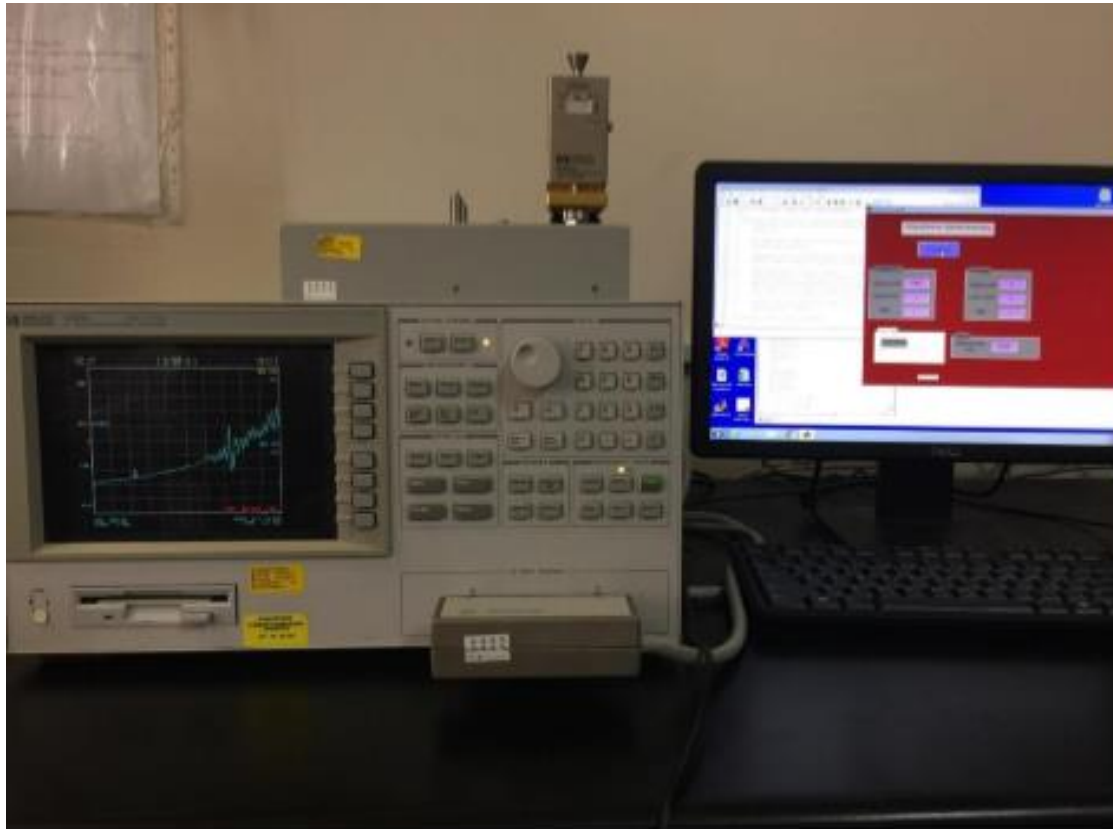


Fig. 3.3: Agilent 4291B RF Signal Generator impedance analyzer.

3.4. Current-Voltage measurements:

The current-voltage (I-V) characteristics were measured by adding two points of carbon (C) on the surface of the samples to change the sample from insulator to conductor. The I-V system which computerized and equipped with a Keithley 6485 pico-ammeter and a Keithley 230

voltage source (Fig.3.4). The Model 6485 Picoammeter has high sensitivity to measure currents less than 1 pA. Even at higher currents, this device makes accurate current measurements. A MATLAB program was used to record the electrical current for voltage ranged from (-100 to +100) volts.

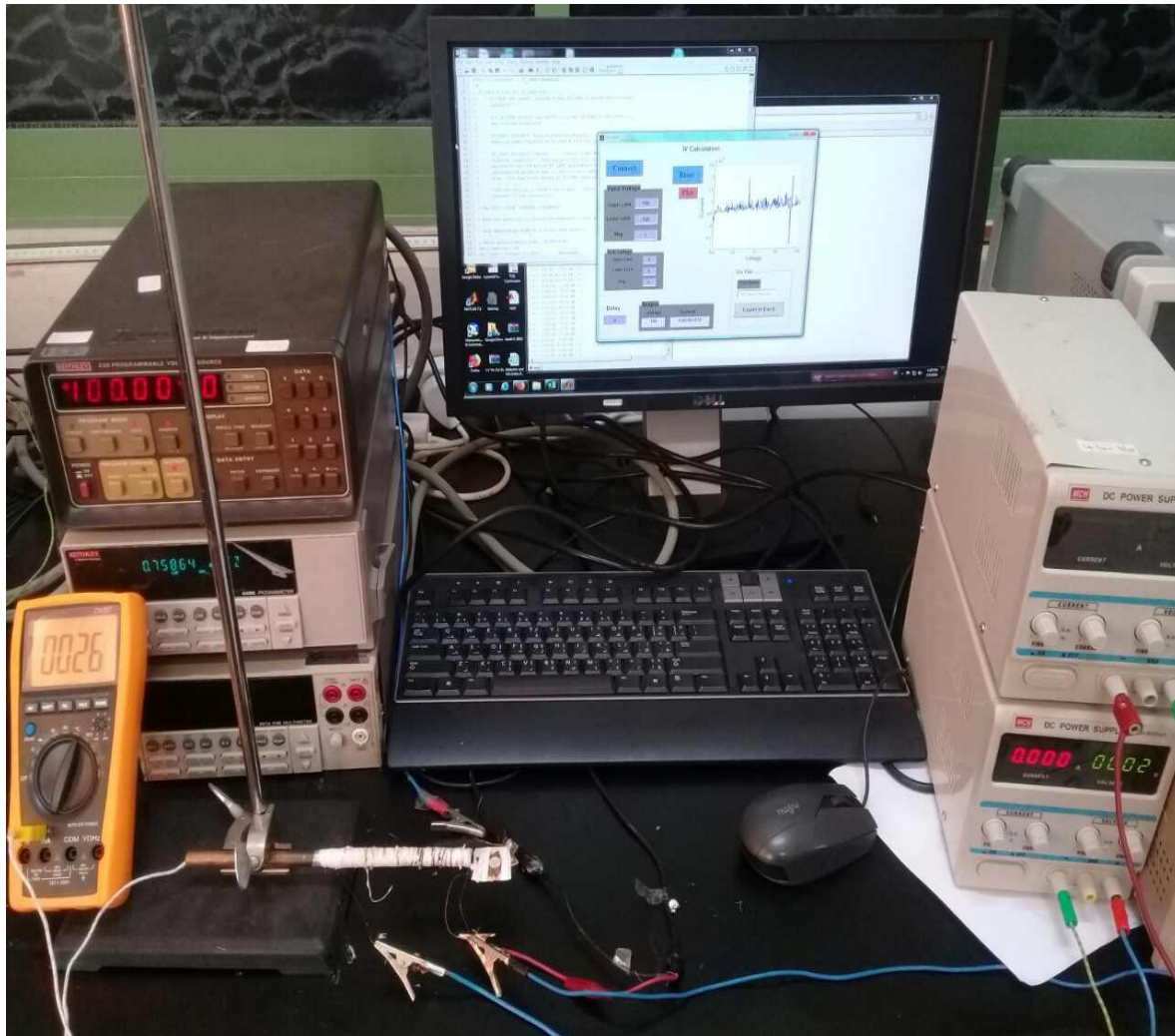


Fig.3.4: The current-voltage device

3.5. Optical measurements:

The optical transmittance spectra were measured using thermo Scientific Evolution 300 spectrophotometer that is equipped with VeeMax II reflectometer in the incident light wavelength range of 300–1100 nm (Fig.3.5). The reflectometer allows measurements at almost normal incidence (15° to normal) and at variable angles in the range of 30 – 80° in 0.1° step. The data were collected and manipulated by means of the VISION software. The transmittance and reflectance measurements were employed to determine the optical band gap, materials absorbability, interband transitions and dielectric dispersion. The T% and R% measurements were carried out in the incident wavelength range of 300– 1100 nm. To measure the transmittance of the BZN pyrochlore ceramics we polished the sample surface 400 revolutions using glass paper and placing the powder of the samples on the adhesive (p 400) and measuring it.



Fig. 3.5: The UV-VIS spectrophotometer.

Chapter Four

Results and Discussion

4.1: Tungsten doping ratio effect on the structural properties

The temperature and doping effects on the structural parameters of BZN is evident from the XRD analysis. Fig.4.1.1 shows XRD diffraction patterns of W doped BZN that is doped in accordance with the empirical formula $\text{Bi}_{1.5}\text{Zn}_{0.92}\text{Nb}_{1.5-6x/5}\text{W}_x\text{O}_{6.92}$ $0.10 \leq x \leq 0.18$. The empirical formula is designed on the basis that the ionic radius of tungsten (~ 0.210 Å) is almost equal that of niobium (~ 0.215 Å) as shown the table (4.1.1) thus the tungsten atoms occupy the sites of niobium atoms by substitution in accordance with the stoichiometry formula $\text{Bi}_{1.5}\text{Zn}_{0.92}\text{Nb}_{1.5-6x/5}\text{W}_x\text{O}_{6.92}$. The diffraction peaks of XRD patterns for all samples are strong and sharp, and the intensities of the peaks are high, indicating a good crystallization of the samples. As table (4.1.2) shows, the intensity of the main peaks of the XRD patterns decreases with increasing doping content in the range of $x = 0.10$ - 0.17 . Namely, the peaks exhibit intensity values of 3237, 1442, 596 and 3910 (a.u.) for $x = 0.10, 0.15, 0.17$ and 0.18 tungsten doped BZN respectively. As illustrated in Fig.1.2 the intensity of BZN decreases from 3237 a.u. to 596 a.u. as doping ratio increases from $x = 0.10$ to $x = 0.17$ and increases to 3910 a.u. at $x = 0.18$. Also, the maximum peak shifts from $2\theta = 30.54^\circ$ to 30.75° as doping ratio increases from $x = 0.10$ to $x = 0.17$ then shifted to $2\theta = 30.46^\circ$ at $x = 0.18$. The number of peaks of W-doped BZN decreases with increasing doping ratio. One possible reason is the tendency of the cubic cell to form pseudo cubic structure at this atomic content value. Similar behavior was also observed for $\text{K}_{0.5}\text{Na}_{0.5}\text{NbO}_3$ (KNN) doped with Sr [28]. The analysis of the X-ray diffraction patterns

indicates that the $\text{Bi}_{1.5}\text{Zn}_{0.92}\text{Nb}_{1.5-6x/5}\text{W}_x\text{O}_{6.92}$ exhibit simple cubic structure. In addition, as shown in table 4.1.1 the spacing of the individual lattice plane is almost constant for all tungsten doped BZN with $x \leq 0.17$. On the other hand, the lattice constant of BZN decreases from 11.70 to 11.62 as x increases from 0.10 to 0.17 then increases to 11.73 at $x = 0.18$.

Table 4.1.1: The ionic radius of the BZN pyrochlore ceramics components.

atom	Ionic radius (nm)
Bi	0.230
Zn	0.139
Nb	0.215
O	0.152
W	0.210

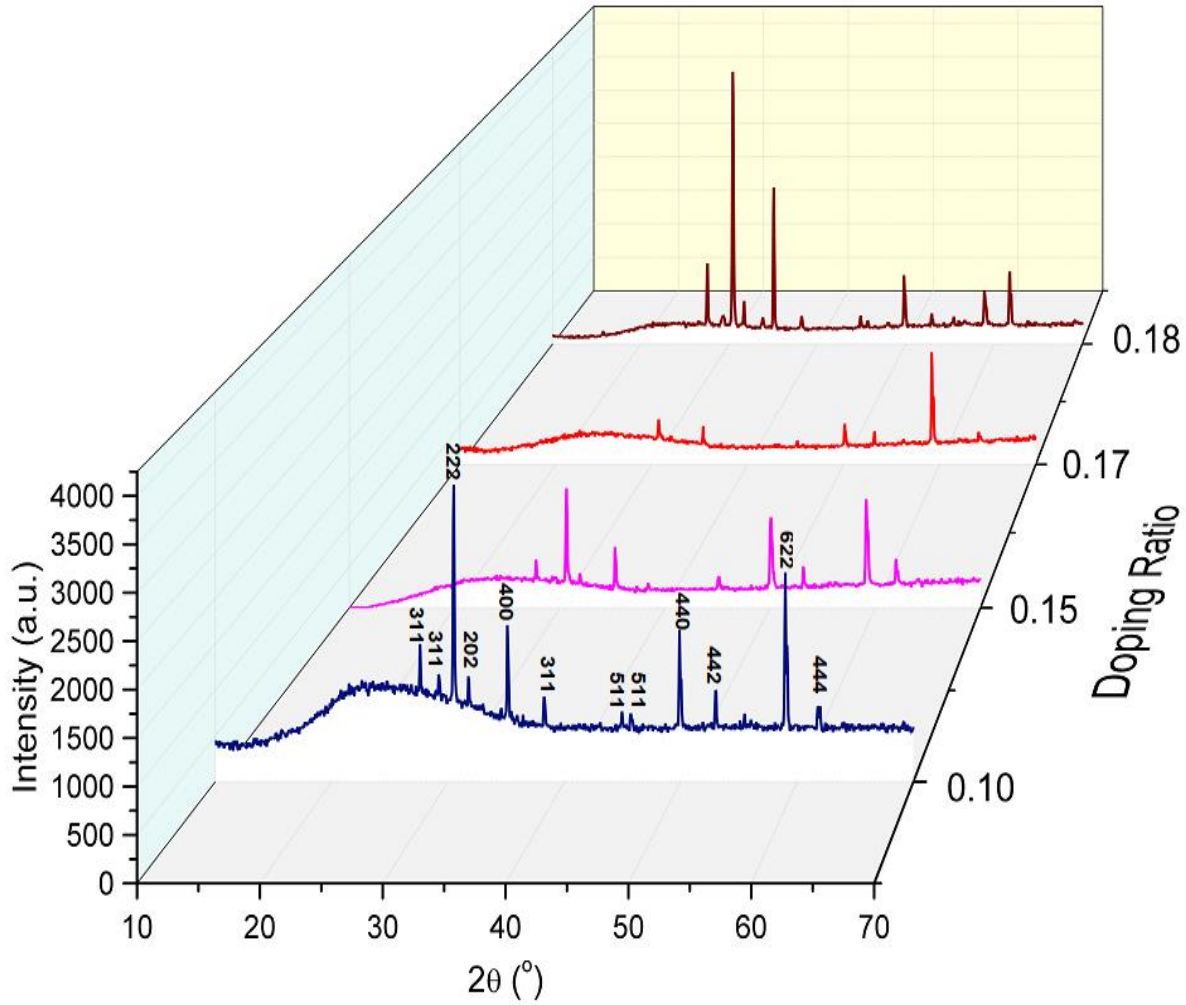


Fig 4.1.1: The 3-D X-ray diffraction patterns from $x= 0.10$ to $x= 0.18$ for $\text{Bi}_{1.5}\text{Zn}_{0.92}\text{Nb}_{1.5-6x/5}\text{W}_x\text{O}_{6.92}$ solid solutions at room temperature.

As shown in table 4.1.2. with x up to 0.17, the intensity (I), interplaner spacing (d) and the average lattice constant (a_{ave}) for the maximum peak at room temperature decreases with increasing the doping ratio. Where, d decreases from 0.292 to 0.290 nm, I decrease from 3237 to 590 (a.u.) and a_{ave} decreases from 11.704 to 11.626 Å with increasing the tungsten doping from $x= 0.10$ to $x= 0.17$.

Table 4.1.2: 2Θ , interplaner space and intensity for maximum peak as a function of W- content for the BZN ceramics at room temperature (298 K).

Doping ratio	2Θ (°)	Interplaner spacing d (nm)	Intensity I (a.u.)	Lattice constant a_{ave} (°A)
0.10	30.54	0.292	3237	11.704
0.15	30.69	0.291	1442	11.648
0.17	30.75	0.290	596	11.626
0.18	30.46	0.293	3910	11.734

As shown in Fig.4.1.2, the intensity of the maximum peak at two diffraction positions of values of $2\theta = 30.54^\circ$ and $2\theta = 59.05^\circ$ for 0.10 sample exhibits lower diffraction angles indicating lattice contraction. By observing the two figures, except for atomic content of $x = 0.18$ which shifts from right to left, as mentioned, these shifts in the peaks indicates a decrease in lattice parameter from $a = 11.704$ °A to $a = 11.626$ °A for $x \leq 0.17$ [29]. Although the intensity of the main peak decreases with increasing doping content, the case is different when the doping ratio reaches 0.18. The increase in the main peak when the pyrochlore exceeds the solubility limit $x = 0.18$ is also observed for $BaCO_3$ ceramics. The behavior is regarded as an abnormal and attributed to the exchange in the atomic substitutions from A to B sites [30]. It is also possible to think that the decomposition of the BZN pyrochlore to Bi_2O_3 , WO_3 and Nb_2O_5 indicate drastically changes in the strain values. This can be concluded from the increase in the lattice constant and the larger

grain size since the peak broadening is inversely proportional to the grain size, larger grains indicate less broadening and as a result sharper XRD diffraction [31]. It could also be due to aggregation of nanoparticles due to the separation of the pyrochlore matrix [32].

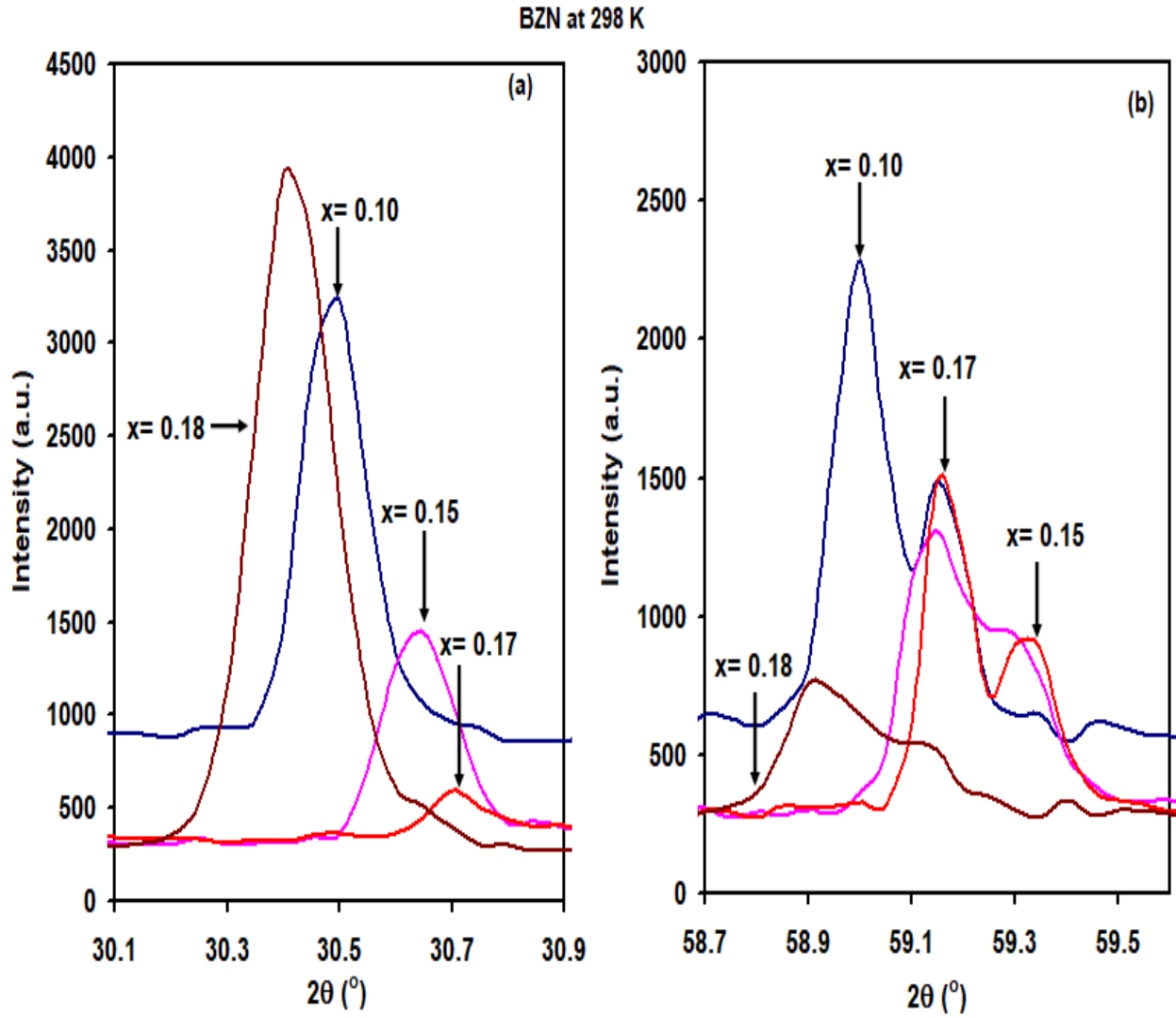


Fig. 4.1.2: The X-ray diffraction patterns for BZN doped with W at diffraction angle of (a) $2\theta = 30.0^{\circ}$ and (b) at $2\theta = 59.0^{\circ}$.

Fig.4.1.3. shows the XRD diffraction at $x = 0.10$ and $x = 0.18$ at room temperature, for a W content of 0.18, new phases appear. The new phases appear at $2\theta = 33.85^\circ$, 49.86° , 56° and 56.8° , with the increased tungsten content of $x = 0.18$. The phases (Table 4.1.3) appear because the pyrochlore reached the solubility limit at $x = 0.18$. The XRD with the help of Treor 92 Software package has shown that the WO_3 could take place as minor phase in the W-doped BZN. The observed 2θ values are also shown in the table. In addition to the appearance of WO_3 appear the Bi_2O_3 and Nb_2O_5 in the structure of BZN.

Table 4.1.3: The materials that can be formed inside W-BZN pyrochlore ceramics and plane.

Code	Material	a	b	c	B	Phases	Plane	Structural
1538317	WO_3	12.1	3.78	23.4	95	33.86 48.71 56.10 56.8	(312) (319) ($\bar{1}27$) (127)	Monoclinic
1545547	Bi_2O_3	7.72	7.72	5.65	90	33.7 49.82	(102) (401)	Tetragonal
2002312	Nb_2O_5	14.20	5.72	5.04	90	33.72	(220)	orthrhombic

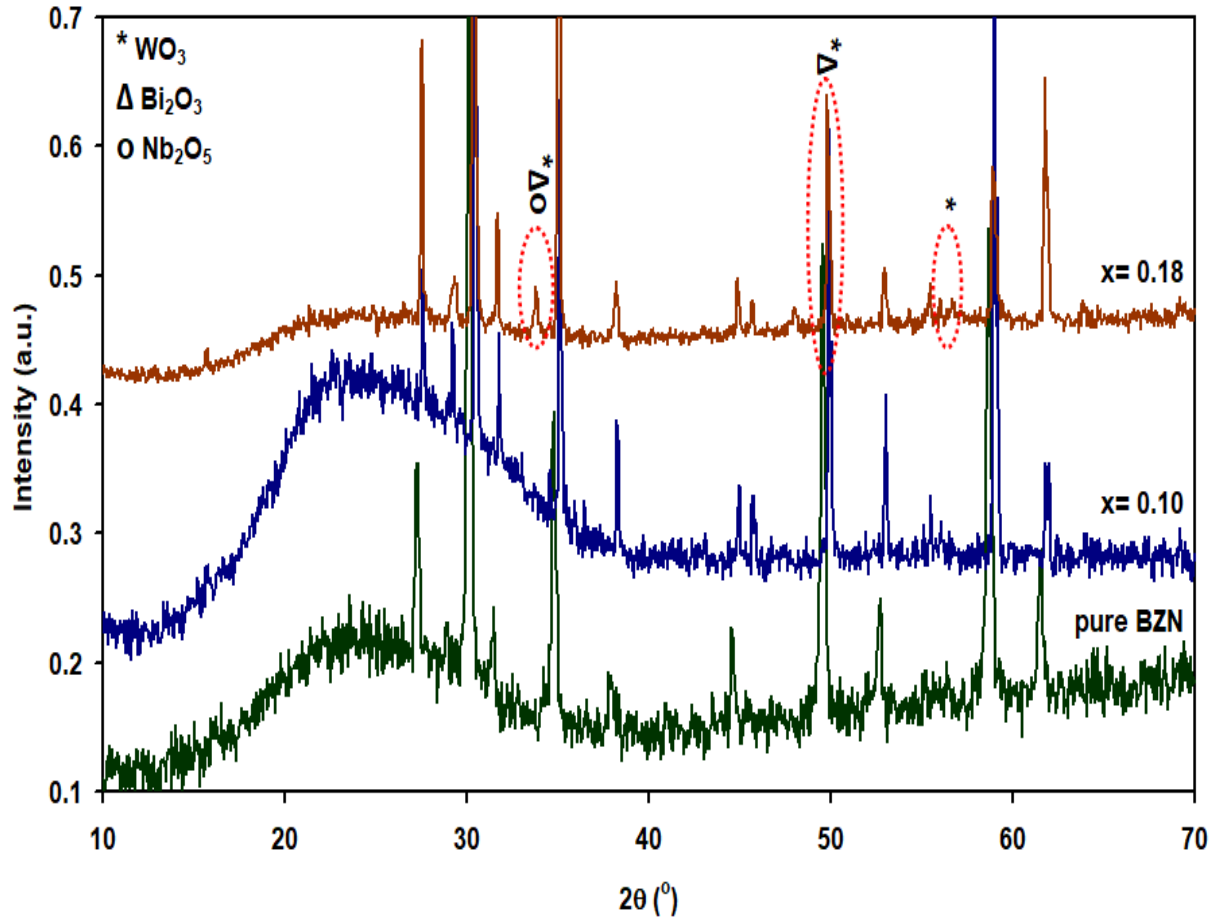


Fig.4.1.3: The X-ray diffraction patterns at pure BZN, $x=0.10$ and $x=0.18$ for $\text{Bi}_{1.5}\text{Zn}_{0.92}\text{Nb}_{1.5-6x/5}\text{W}_x\text{O}_{6.92}$ solid solutions at room temperature.

The mechanical properties are also studied as a function of the doping ratio. Particularly, the crystallite size, the micro strain, the dislocation density, degree of orientation and the lattice constant are all calculated from the observed 2Θ and the peak broadening at full wave half maximum (FWHM). The results are tabulated and plotted in Fig.4.1.4 and table 4.1.4. Fig.4.1.4 shows the variation in better way. Fig.4.1.4 (a) presents the values of crystallite size being

calculated with the help of equ. (2.20) from the main peak which is oriented in the (222) at $2\theta=30.0^\circ$ and (622) directions at $2\theta=59.0^\circ$.

As shown in the figure, the crystallite size has three regions of variation with increasing doping ratio. It starts at value of $D= 57\text{nm}$ and remains constant from $x= 0.10$ to $x= 0.15$, then sharply increases for $x= 0.17$ and it exhibits sharp fall in the D value reaching 25 nm at $x= 0.18$, where it becomes pseudo cubic structure. The increase in the crystallite size of tungsten doped samples creates a stress on the crystallites of the pyrochlore leading to increasing compressing strain, increasing dislocation density and decreasing lattice constant -at $D= 200\text{ nm}$ is valid-. The calculated strain values are of the order of 10^{-3} and are of negative sign indicating a compressive strain type in the structure [33]. Fig 4.1.4 (b) shows the average absolute strain as a function of the doping ratio.

Table 4.1.4: The mechanical parameters of the maximum peak as a function of W content for the BZN ceramics at room temperature (298 K).

Doping ratio	Lattice constant a ($^\circ\text{A}$)	Strain $\epsilon \times 10^{-3}$	Crystallite size D (nm)	Dislocation density $\delta \times 10^{11}$	Degree of orientation K
0.10	11.704	2.397	57	3.34	0.190
0.15	11.648	2.385	57	3.33	0.114
0.17	11.626	1.586	860	1.48	0.134
0.18	11.734	5.449	25	17.21	0.364

The strain constant for $x \leq 0.15$. For larger values of x , it decreases slowly with increasing doping ratio then it sharply increases at $x = 0.18$. Fig 4.1.4 (c) illustrates the dislocation density being calculated by equation (2.28), which represents an imperfection in a crystal associated with the misregister of the lattice in one part of the crystal with the other part. Increasing the tungsten content in the pyrochlore ceramics increases the dislocation density. The strain and dislocation density follows the same behavior. It always increases with increasing tungsten content in the $\text{Bi}_{1.5}\text{Zn}_{0.92}\text{Nb}_{1.5-6x/5}\text{O}_{6.92}$. The two parameters ϵ and δ are of lattice misfit origin that depends upon sample preparation conditions [34]. The dislocation density is calculated by using equation (2.28).

The degree of remains orientation that is calculated using both the intensity of the maximum peak and the summation of the intensities of all observed diffraction peaks is illustrated in Fig 4.1.4 (d). The degree of orientation decreases slowly with increasing the tungsten doping content in the range of 0.10-0.17 and then sharply increases when the doping ratio reaches 0.18.

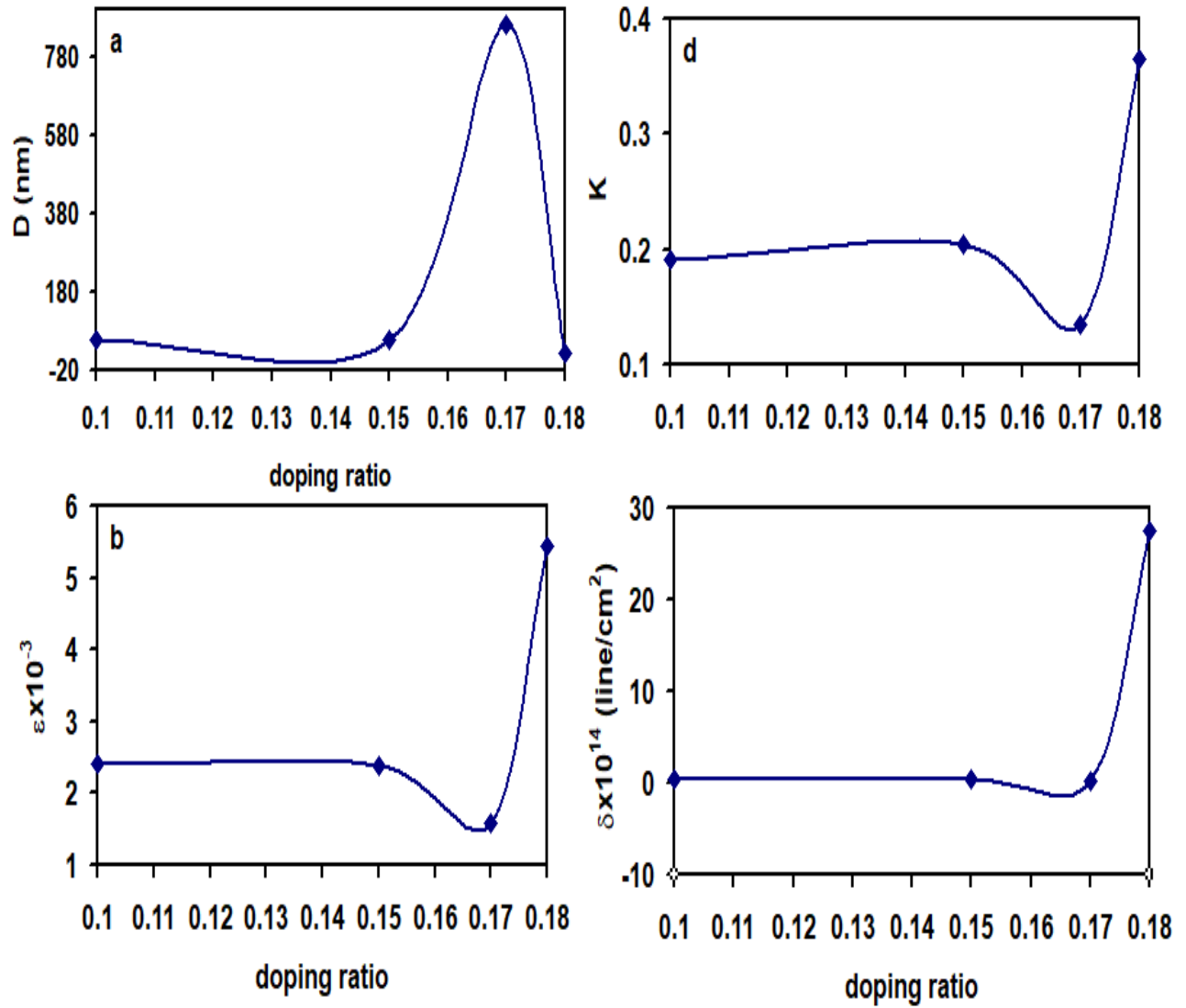


Fig 4.1.4: (a) crystallite size (b) Strain (c) Dislocation density (d) degree of orientation (K) for W doped BZN pyrochlore ceramics.

Fig.4.1.5 reflects the effects of W doping on the lattice constant of the doped pyrochlore. As clarified in the figure, the lattice constant decreases smoothly from 11.70 Å to 11.62 Å as the doping ratio increases from 0.10 to 0.17. The slight attenuation that occurs in the lattice constant

is probably due to the smaller ionic radius of W (2.10 Å) compared to that of Nb (2.15 Å) [35]. At $x = 0.18$ the lattice constant sharply increases to 11.73 Å. The increase in the lattice constant for samples doped with W of content at $x = 0.18$ is due to the minor phases of WO_3 , Nb_2O_6 and Bi_2O_3 . The crystalline nature is destroyed at this limit and the material comprises these minor phases as agents which forces the pyrochlore to exhibit different structural characteristics.

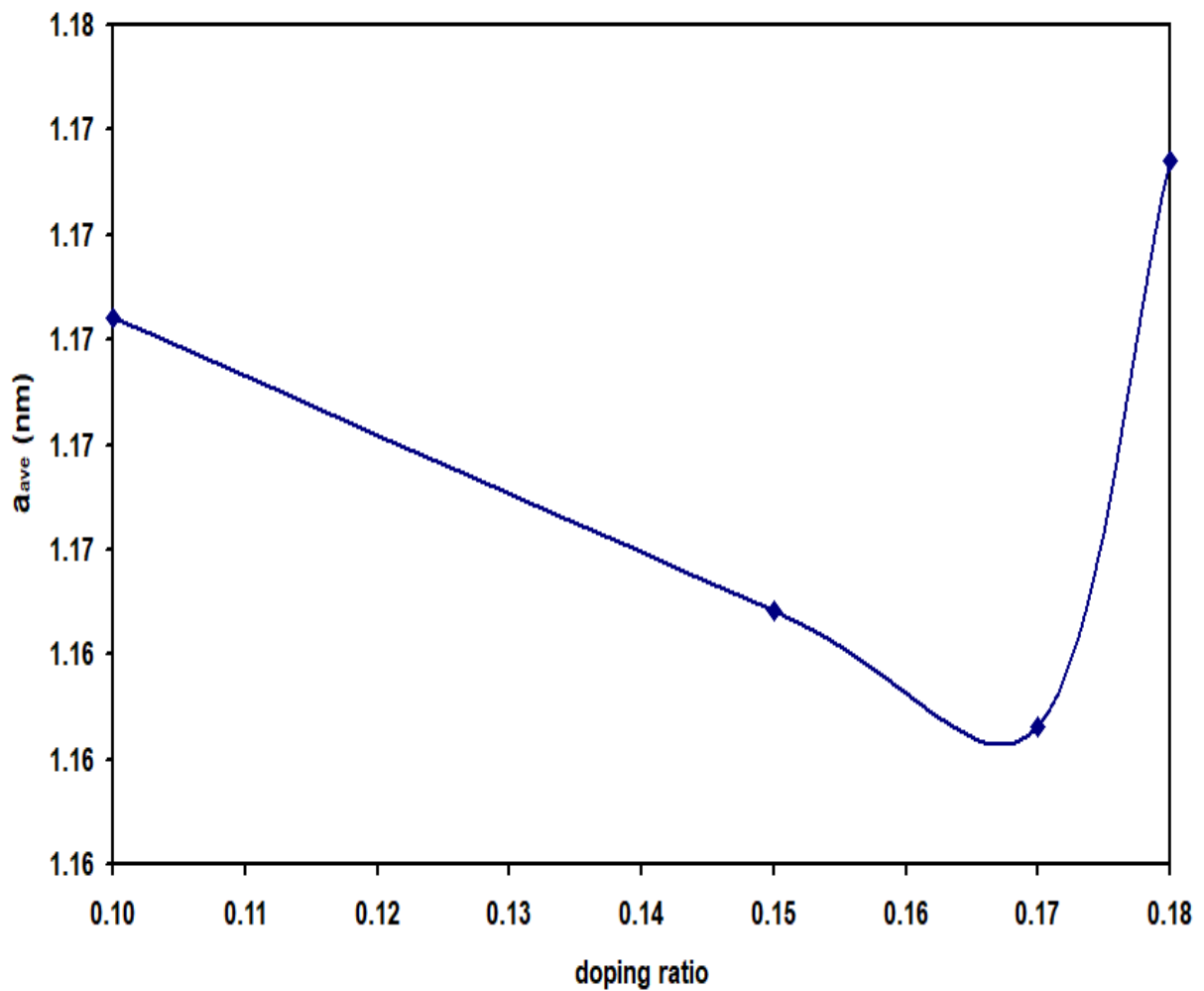


Fig.4.1.5: Variation of the lattice constant with W content

4.2: Temperature dependent XRD analysis for $\text{Bi}_{1.5}\text{Zn}_{0.92}\text{Nb}_{1.5}\text{W}_x\text{O}_{6.92}$

The XRD of the $\text{Bi}_{1.5}\text{Zn}_{0.92}\text{Nb}_{1.5-6x/5}\text{O}_{6.92}$ with $x = 0.17$ and $x = 0.18$ pyrochlore ceramics, were studied in the temperature range of 298-474 K. There are two maximum peaks which exist in this doped sample. For simplicity, two high intensity peaks are selected in this doped sample at $2\theta = 30.2^\circ$. Fig.4.2.1 shows the two maximum peaks at each temperature. The intensity of the maximum peak increases from 953 to 1665 (a.u.) as temperature increases from 298 to 428 K then it follows an oscillating but comparatively decreasing tendency.

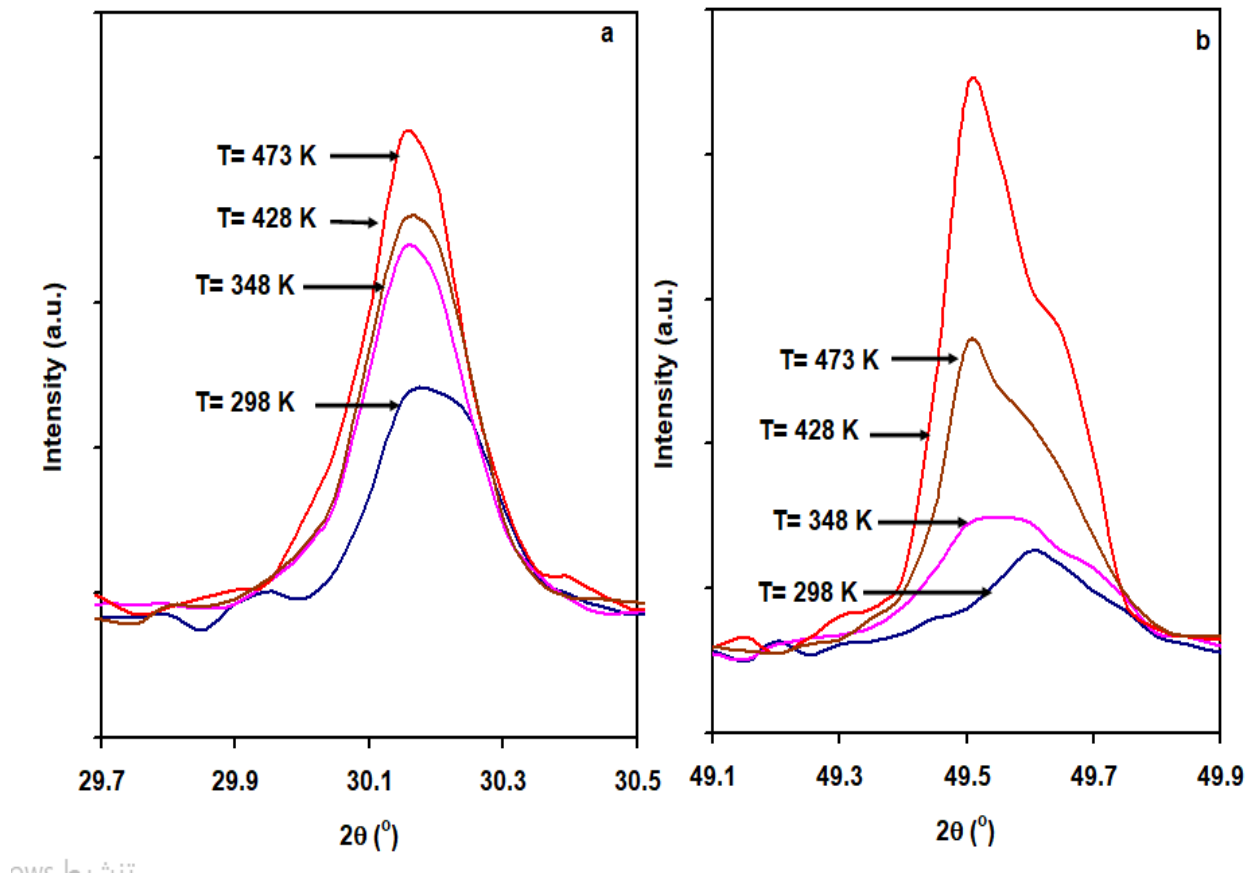


Fig. 4.2.1: The X-ray diffraction patterns at $x=0.17$ for $\text{Bi}_{1.5}\text{Zn}_{0.92}\text{Nb}_{1.5-6x/5}\text{W}_x\text{O}_{6.92}$ solid solutions at $2\theta=30.2^\circ$ and at $2\theta=49.7^\circ$ as a function of temperature.

Fig.4.2.2 shows the mechanical properties for W-BZN of the content of $x=0.17$ as a function of temperature for the maximum peak. A mechanical property of the maximum peak is different in their behavior when increasing temperature. Fig.4.2.2.a displays the crystallite size for the sample. As illustrated in the figure, the crystallite size exhibit two regions of variations, presented by an increases in the crystallite size as temperature increase up to 380 K. On the other hand, the strain which appears in Fig.4.2.2.b with ignoring the value of strain at 323 k. The strain follow an increasing trend of variation followed by a decreasing trend below and above 383 K, respectively. Fig.4.2.2.c shows the dislocation density of the W-BZN at $x=0.17$ for the maximum peak. The dislocation density has the same behavior as the strain at the same values in both the maximum peak.

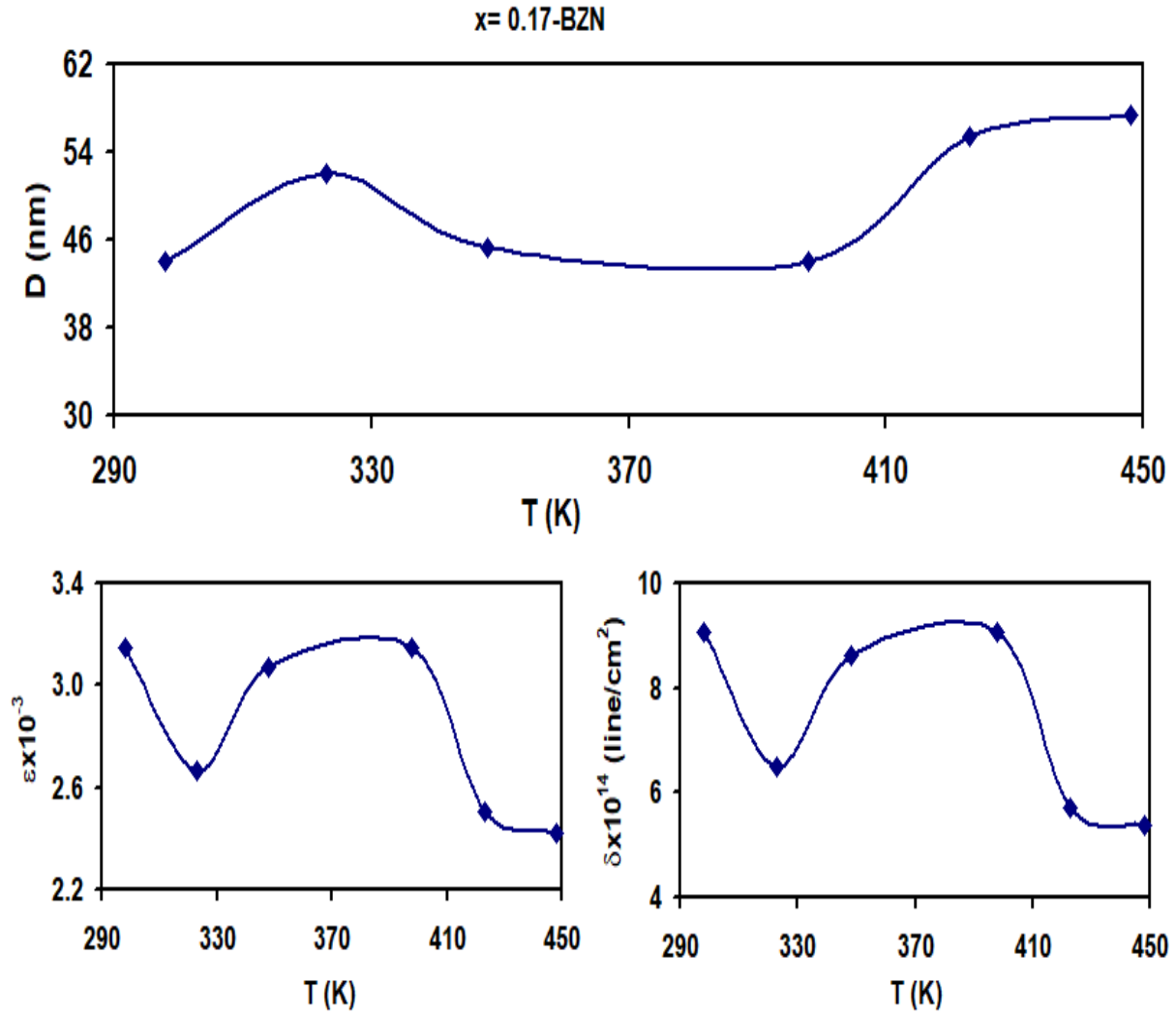


Fig 4.2.2: (a) Crystallite size (b) Strain (c) Dislocation density of W-BZN as a function of temperature for $x = 0.17$

Fig.4.2.3 displays the X-ray diffraction patterns which were recorded with temperature for W-BZN pyrochlore ceramics of the content of $x = 0.18$. As the figure shown, there are seven peaks apparent at each temperature. The indexing of the diffracted intensive peaks was performed using the indexing method of cubic structure as given by Cullity [29]. The diffraction peaks at

room temperature for the content of $x = 0.18$ at 2θ value of 27.59° , 30.46° , 31.75° , 35.08° , 49.86° , 58.98° and 61.83° were indexed corresponding to the planes (311), (222), (400), (331), (440), (622) and (444), respectively. In addition, these peaks increase and decrease randomly as the temperature increases. As interesting feature, a maximum intensity of value of 7928 (a.u.) was observed at $2\theta = 30.45^\circ$ when the temperature reached 373 K.

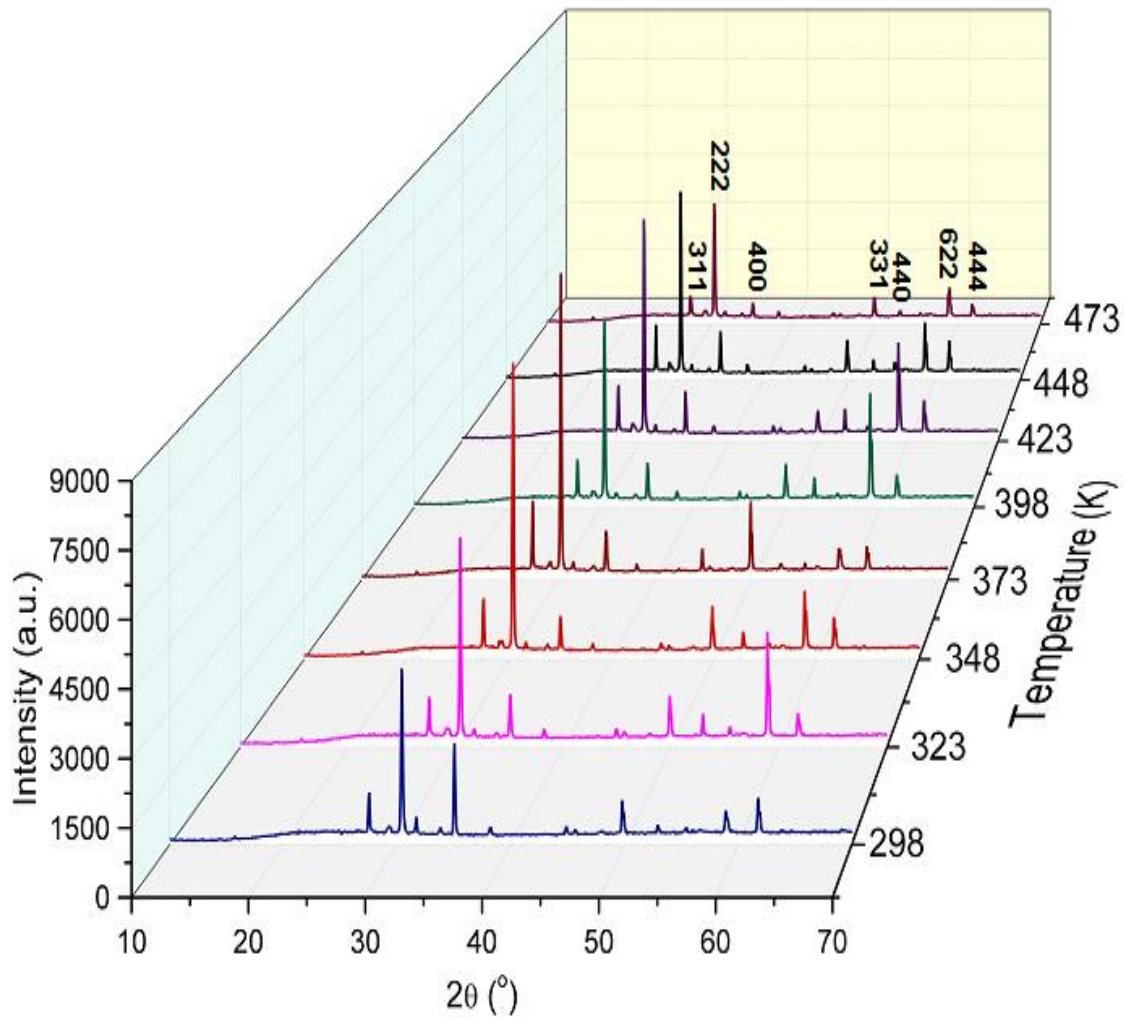


Fig. 4.2.3: X-ray diffraction patterns for $\text{Bi}_{1.5}\text{Zn}_{0.92}\text{Nb}_{1.5-6x/5}\text{W}_x\text{O}_{6.92}$ with $X = 0.18$ as a function of temperature.

Fig.4.2.4 shows the intensity of the maximum peak at each temperature. The intensity of the maximum peak increases and decreases with increasing temperature. Particularly, the intensity of the maximum peak increases from 3910 to 7928 (a.u.) as temperature increases from 298 to 373 K then it follows a fluctuating but relatively decreasing trend of variation. As also seen, the peaks systematically shift toward lower 2θ values. This systematic shift is an indication of uniform deformation or recrystallization. The recrystallization is defined as the formation of new, strain-free, equiaxed crystallites from previously strain-hardened crystallites. In the recrystallization process, the deformed grains are replaced by a new set of undeformed grains that nucleate and grow until the original grains have been entirely consumed [34].

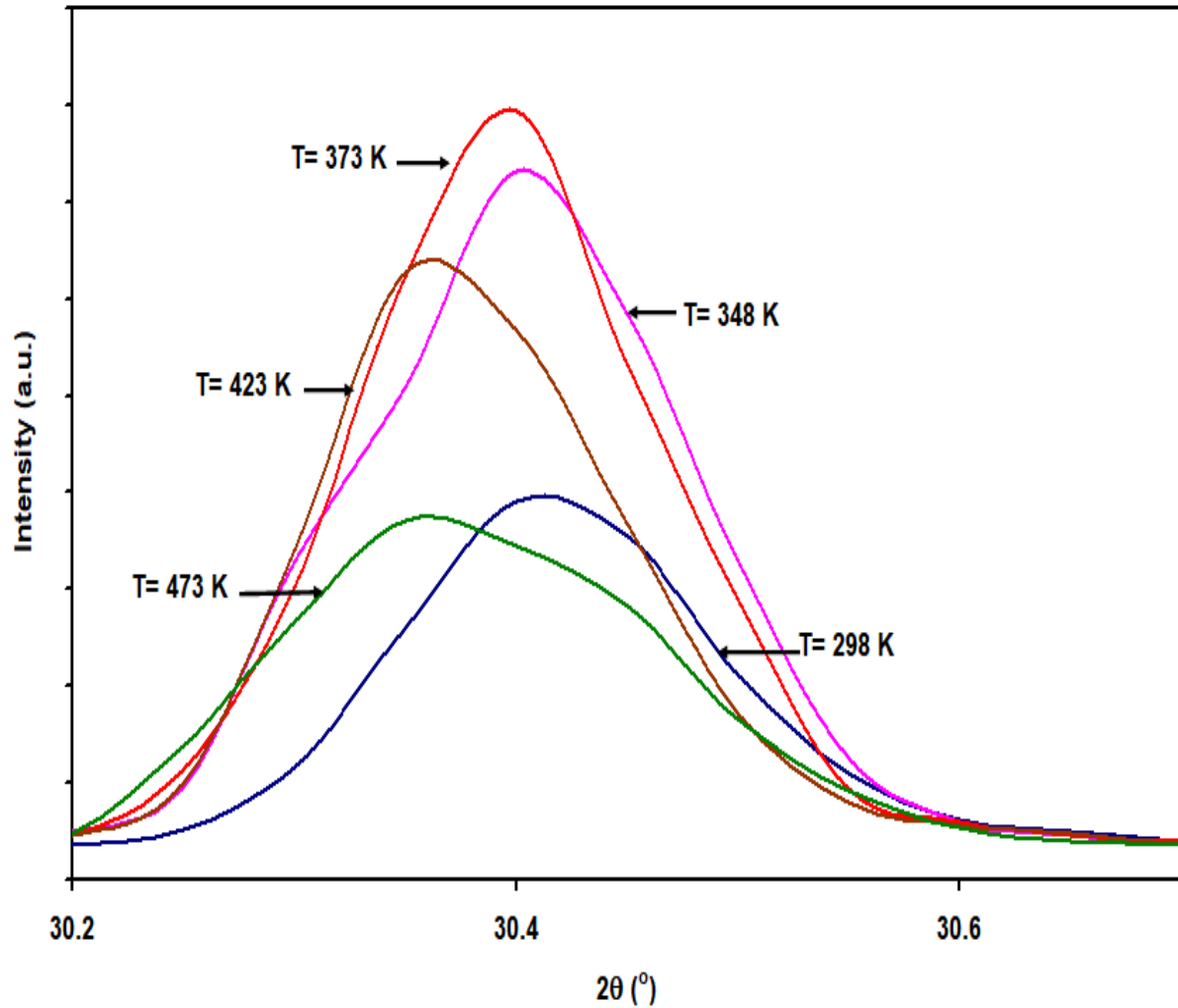


Fig. 4.2.4: The X-ray diffraction patterns at $x=0.18$ for $\text{Bi}_{1.5}\text{Zn}_{0.92}\text{Nb}_{1.5-6x/5}\text{W}_x\text{O}_{6.92}$ solid solutions at $2\theta=30.4^{\circ}$ as a function of temperature.

Fig.4.2.5. presents the intensity of the maximum peak before and after heating. The intensity of the maximum peak for the sample after heating which is equal to 4019 (a.u.) is a bit larger than before heating which was equal to 3910 (a.u.). It is clear from the figure that the BZN pyrochlore stability at larger diffraction angles indicates smaller interplanar spacing and smaller lattice parameters. Also, the XRD of the samples before and after heating did not cause the

emergence of new phases. The breadth of the maximum peak is larger after heating than before heating case.

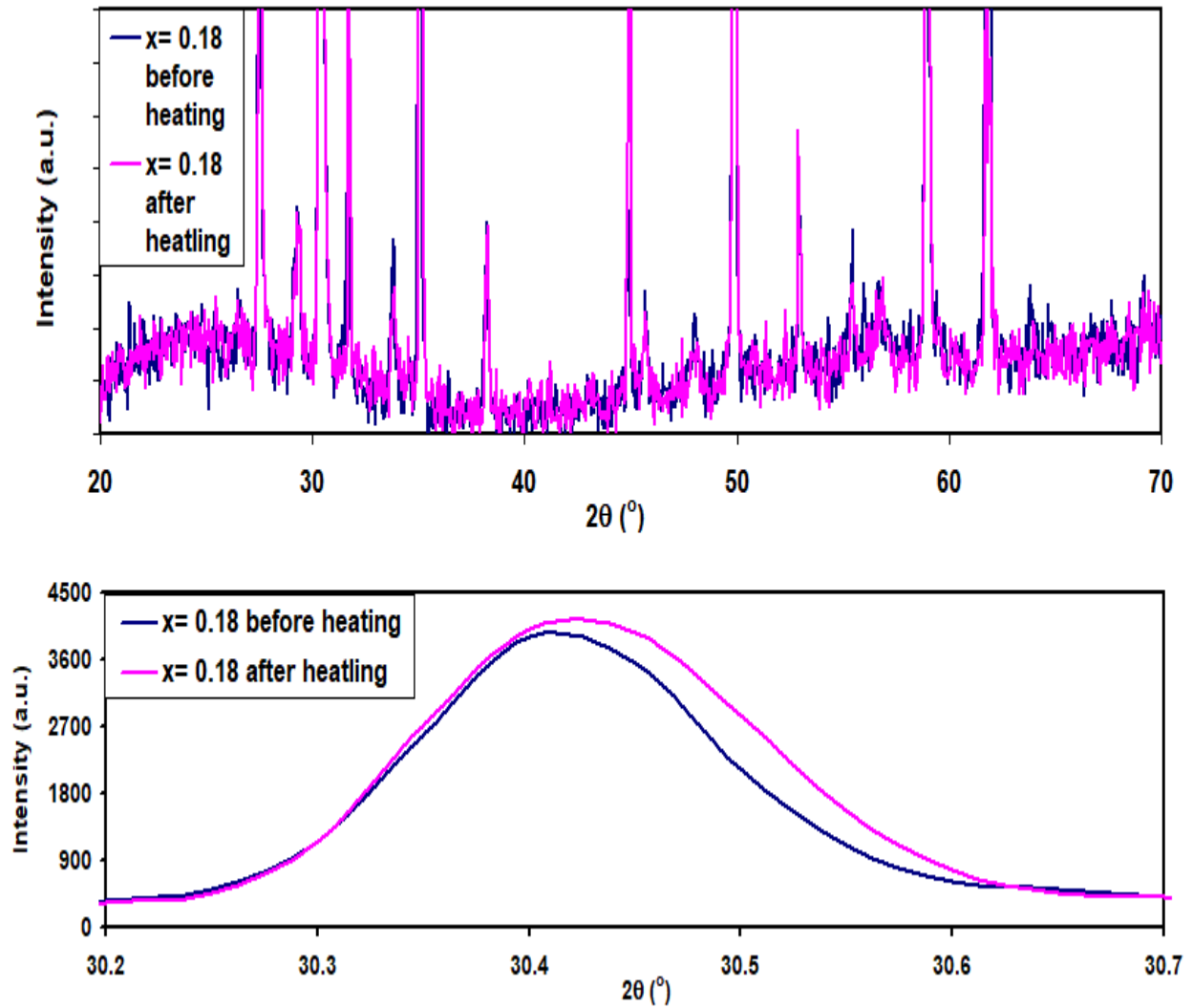


Fig. 4.2.5: The X-ray diffraction patterns at $x=0.18$ for $\text{Bi}_{1.5}\text{Zn}_{0.92}\text{Nb}_{1.5-6x/5}\text{W}_x\text{O}_{6.92}$ solid solutions at $2\theta=30.4^\circ$ for the temperature of before and after heating

The mechanical properties for this sample were studied with temperature from 298 K to 473 K as shown in Fig.4.2.4. The crystallite size of W-BZN pyrochlore ceramics follows two regions of variation 298-423 K and 448-473 K. In the region of 298-423 K, the crystallite size decreases due to re-stabilization forced by internal energy and re-decrease to 44.47nm in the region of 448-473 K. The strain decreases from 1.89×10^{-3} at 298 K to 1.52×10^{-3} at 323 K and increases to 1.92×10^{-3} at 373 K. In addition, the strain re-increased to 2.33×10^{-3} at 473 K. The behavior of dislocation density and strain is the same. The dislocation density decreases from 0.64×10^{11} line/cm² at 298 K to 0.34×10^{11} line/cm² at 323 K and increases to 0.58×10^{11} line/cm² at 373 K, then the dislocation density re-increases to 0.79×10^{11} at 473 K. The reason is possibly due to the reducing in the internal energy to achieve the stability case. The decrease in dislocation density relates to decrease in the strain [36]. The degree of orientation is increases in the two regions 298-348 K and 398-473 K. In the region of 298-348 K, the degree of orientation increases from 0.364 to 0.499 and increases from 0.372 to 0.449 in the region of 398-473 K.

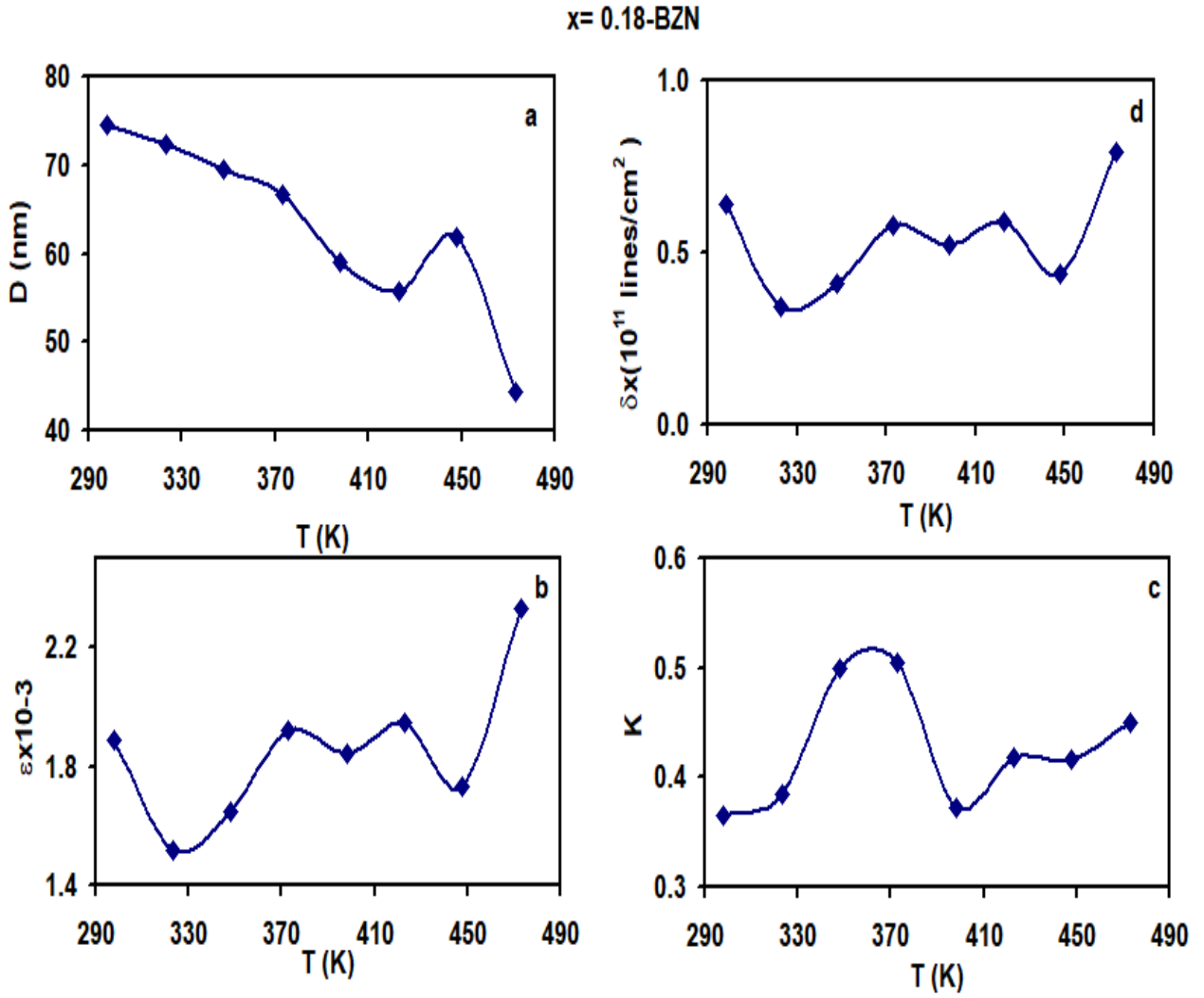


Fig 4.2.6: (a) Crystallite size (b) Strain (c) Dislocation density (d) degree of orientation of W-BZN as a function of temperature for $x = 0.18$.

4.3: Scanning Electron microscopy and energy dispersive X-ray analysis

The scanning electron microscopy images for the W-doped BZN are measured for sample's which were doped with W of content of $x=0.17$ in Fig.4.3.1 and $x=0.18$ in Fig. 4.3.2 in accordance with the empirical formula $\text{Bi}_{1.5}\text{Zn}_{0.92}\text{Nb}_{1.5-6x/5}\text{W}_x\text{O}_{6.92}$. The image for a 15000 enlargement of the sample doped with W of 0.17 displays single phase of the pyrochlore ceramics with no additional phases. For $x=0.17$ the grain size was found to range from 2 to 6 μm . On the other hand, the crystallite size observed from XRD measurements is about $\sim 0.9 \mu\text{m}$. This indicates that each grain of W-BZN comprises many crystallites percolates together. For $x=0.18$ also large grain size that contains so many crystallites were observed. The grains are very large and comprise many crystallites. On the other hand, the scanning electron microscopy analysis for the samples doped with W content of $x=0.18$ has shown that there exist more than one structural phases in the pyrochlore. The image shows in Fig.4.3.2 (a) displays some bright borders around the grains. The enlargement of 5000 times of these two regions is shown in Fig.4.3.2 (b). The two points were selected and tested by the energy dispersive X-ray analyzer (EDS). The EDS analysis of point 1 reveals the presence of Bi_2WO_6 as minor phase in the structure of the pyrochlore ceramics. The analysis of point 2 reveals the BZN pyrochlore itself. In the light of these analysis it is possible to guess that the pyrochlore ceramics exceeds the solubility limit when a doping content of $x=0.18$ is reached. Since at $x=0.18$ we observe minor extra phases other than those for BZN, $x=0.17$ can be considered to be the solubility limit of W into the BZN crystal structure.

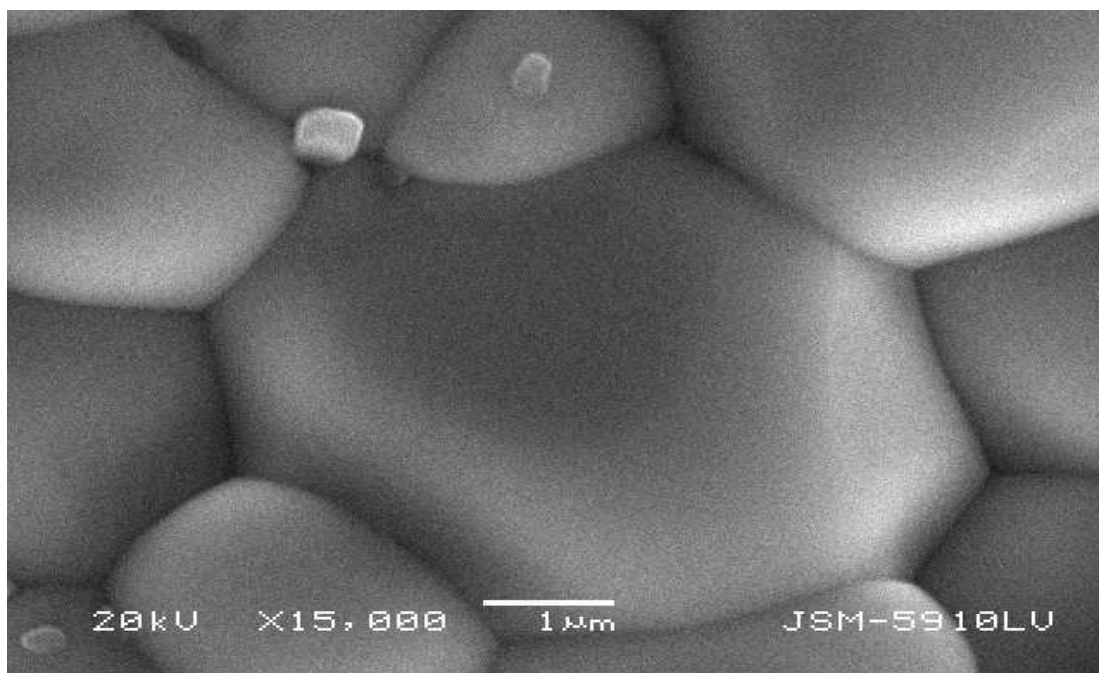


Fig.4.3.1: The scanning electron microscopy images for the $\text{Bi}_{1.5}\text{Zn}_{0.92}\text{Nb}_{1.5-6x/5}\text{W}_x\text{O}_{6.92}$ pyrochlore composition of $x=0.17$ being enlarged 15000 times.

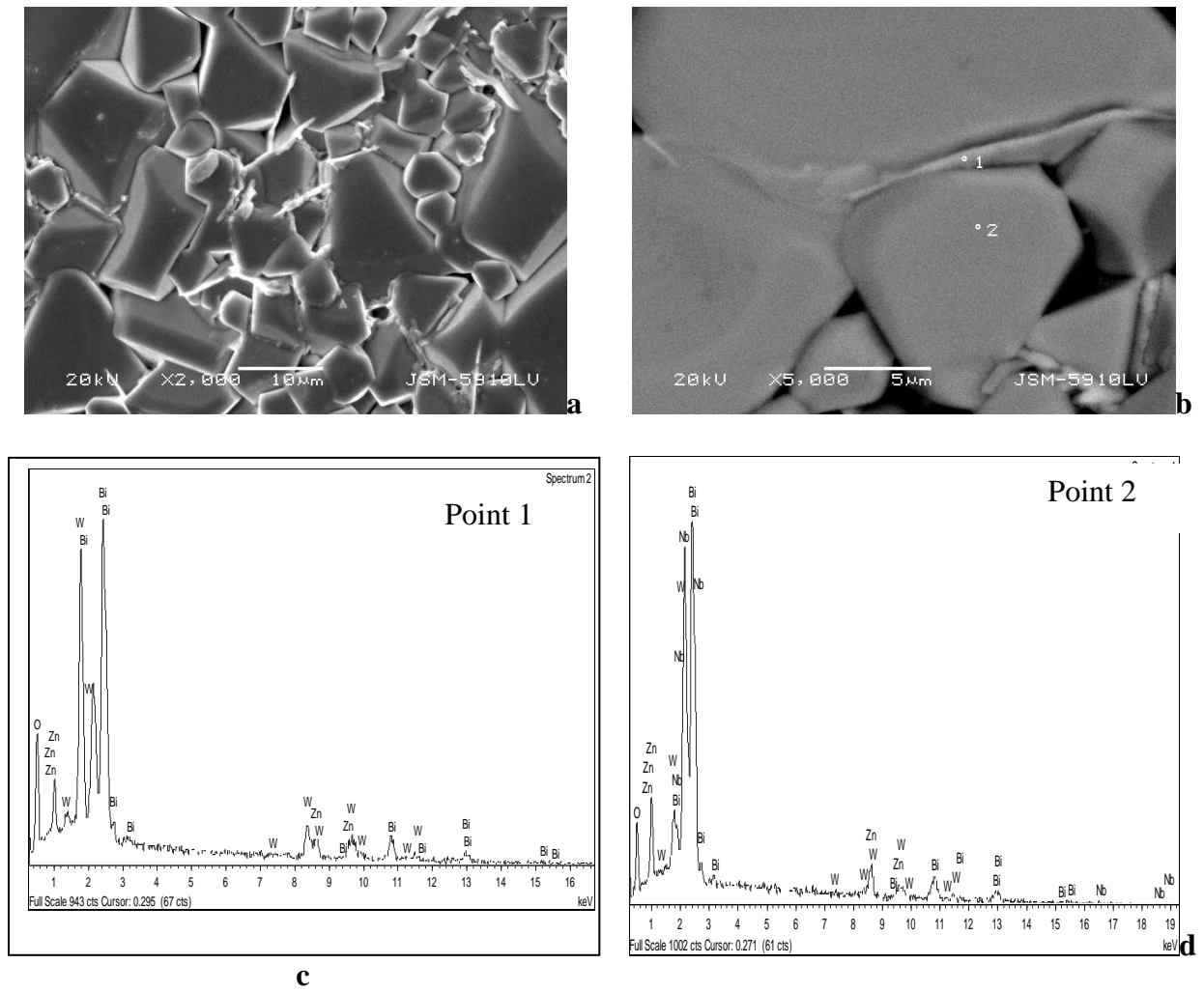


Fig.4.3.2: The scanning electron microscopy images for $\text{Bi}_{1.5}\text{Zn}_{0.92}\text{Nb}_{1.5-6x/5}\text{W}_x\text{O}_{6.92}$ pyrochlore ceramics doped with tungsten of content of $x=0.18$ (a) enlargement of 2.000 times b) enlargement of 5000 times, c) point 1 EDS analysis showing that the W-doped BZN exceeds the solubility limit with the presence of Bi_2WO_6 and d) point 2 the EDS analysis showing the pyrochlore itself.

4.4: Impedance spectroscopy of W doped BZN:

The electrical properties of W-BZN as a function of doping ratio are studied in the frequency range of 0.01-1.80 GHz. The capacitance spectra of $\text{Bi}_{1.5}\text{Zn}_{0.92}\text{Nb}_{1.5-6x/5}\text{W}_x\text{O}_{6.92}$ pyrochlore ceramics are presented in Fig.4.4.1. As seen from the figure, the capacitance at the content of $x=0.10$ decreases with increasing the frequency. When the W content is increases to 0.15 the capacitance also increases in the region of 0.01-1.6 GHz and decreases in the region of 1.6-1.8 GHz. Raising W content to $x=0.17$ forced the BZN to exhibit different characteristics. Namely, it exhibits resonance-antiresonance characteristics at 0.42 GHz. Then it shows a decay followed by negative capacitance effect at 1.23 GHz. The negative capacitance continues until a frequency value of 1.32 GHz is reached where it then becomes positive. On the other hand, the capacitance spectra for the sample doped with W of content of $x=0.18$ displays a resonance-antiresonance character in the range of 1.2-1.4 GHz. This phenomenon is followed by negative capacitance effect in all the studied range. The resonance peaks are following each other. The property with this style is useless as it doesn't allow stable data transfer when used as microwave resonator. The reason of this strange behavior is assigned to the presence of many phases in the sample which have different modes of oscillation.

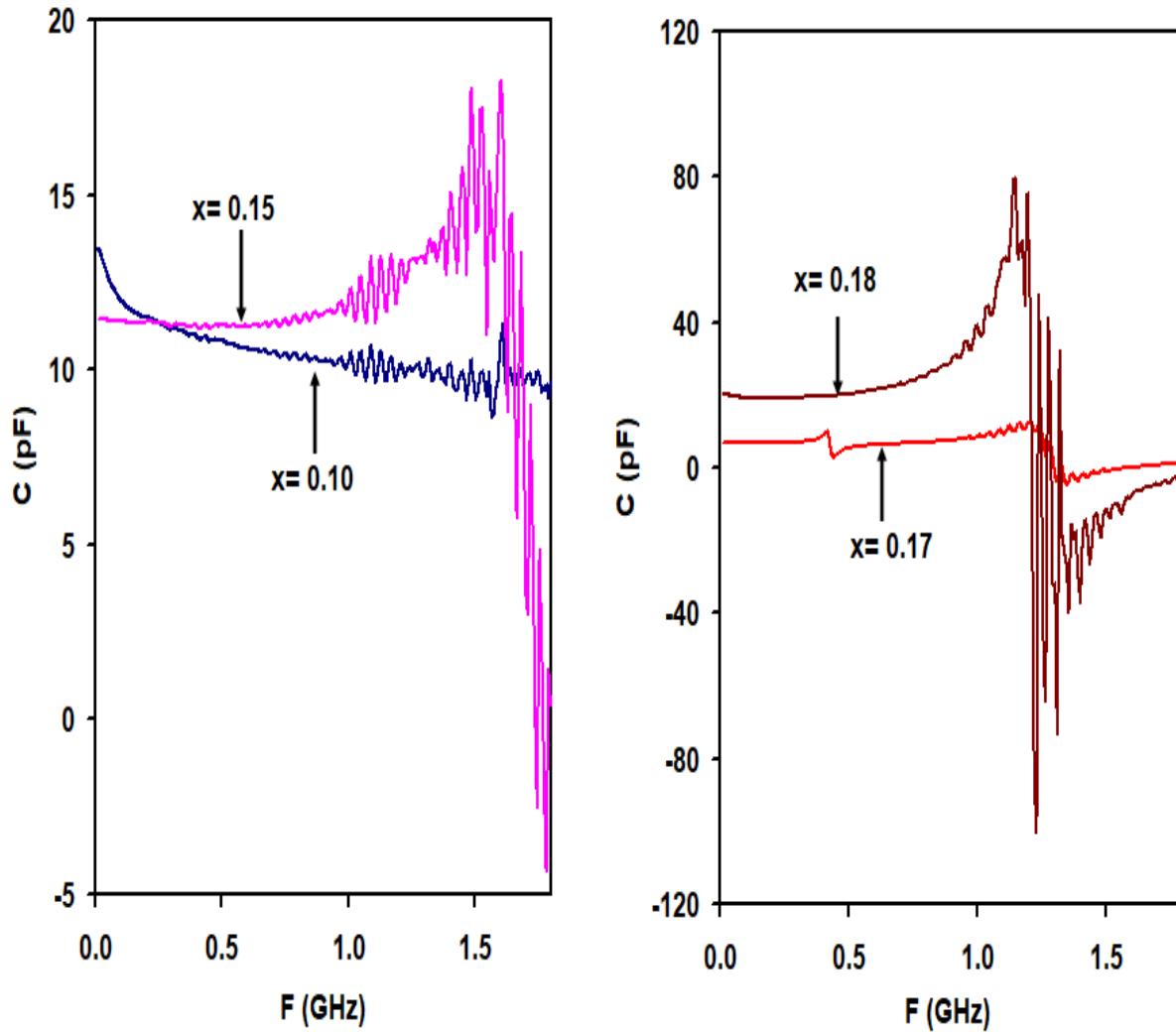


Figure 4.4.1

Fig.4.4.1: The capacitance spectra for $\text{Bi}_{1.5}\text{Zn}_{0.92}\text{Nb}_{1.5-6x/5}\text{W}_x\text{O}_{6.92}$ pyrochlore ceramics being registred at room temperature

The conductance spectra (Fig.4.4.2) are measured for all doped samples. The conductance of the content of $x=0.10$ shows two distinct incremental trends below and above 0.7 GHz. The conductance for W-content of $x=0.15$ has the same behavior of $x=0.10$ except for the sharper

slope of increase at high frequency. In addition, the conductance for W-content of $x=0.17$ has three peaks. The best response appears at 1.59 GHz. The conductance spectra of W-doped BZN with $x=0.18$ have a peak at 1.23 GHz then exhibit unstable trends of variation.

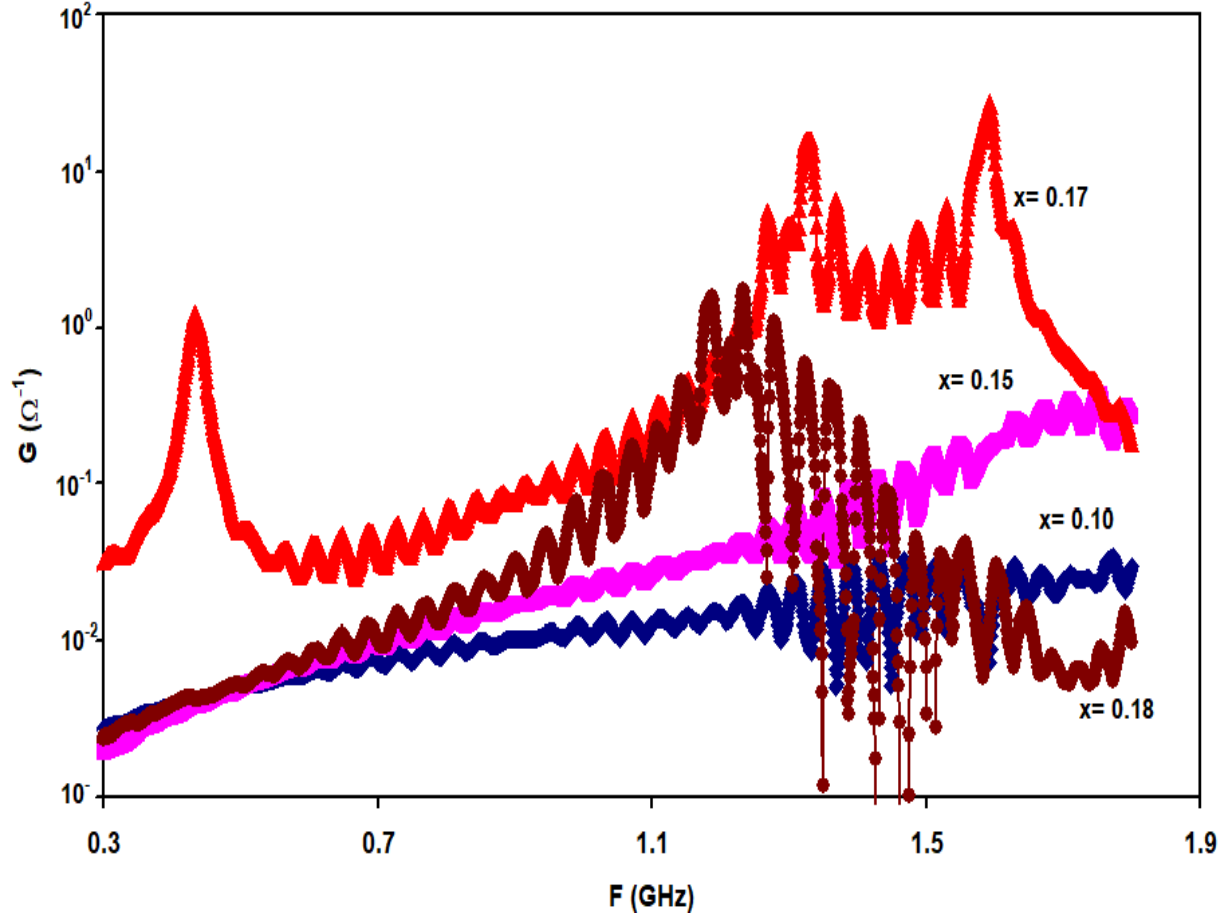


Fig.4.4.2: The Conductance of W-BZN as a function of frequency.

In order to get better illustration of microstructural electroactive regions in the samples, the total impedance is calculated. The impedance is actually the total resistance offered by the sample to the flow of AC current. Fig.4.4.3. presents the impedance of BZN doped with tungsten. The

impedance for the W-content of $x = 0.10$ and $x = 0.15$ has the same behavior which is presented by fast decay followed by slowly varying trends. The fast decay exists in the range of 0.01-0.19 GHz and the smoother one in the range of 0.19-1.80 GHz. In addition, the impedance for the W-content of $x = 0.17$ decreases by three orders of magnitude upon frequency increasing. The impedance exhibits two minima at frequency positions of 0.42 GHz and 1.28 GHz. The minimum value of the impedance is reached at a frequency of 1.28 GHz. For signal frequencies greater than this value, the impedance increases sharply with increasing frequency. The behavior of the BZN pyrochlore ceramics in the region of frequency above 1.28 GHz indicates its applicability as band stop filter [37]. The impedance of the W-content of $x = 0.18$ decreases from 741.02 Ω at 0.01 GHz to 1.09 Ω at 1.23 GHz then increases to 33.80 Ω at 1.8 GHz. The minimum value of the impedance is reached at a frequency of 1.23 GHz. The remaining part of impedance data is not shown in the figure due to its unstable style of variation which makes data observation impossible. This behavior of impedance and conductance at W-content of $x = 0.18$ is attributed to the presence of minority phases as the material exceeds the solubility limit.

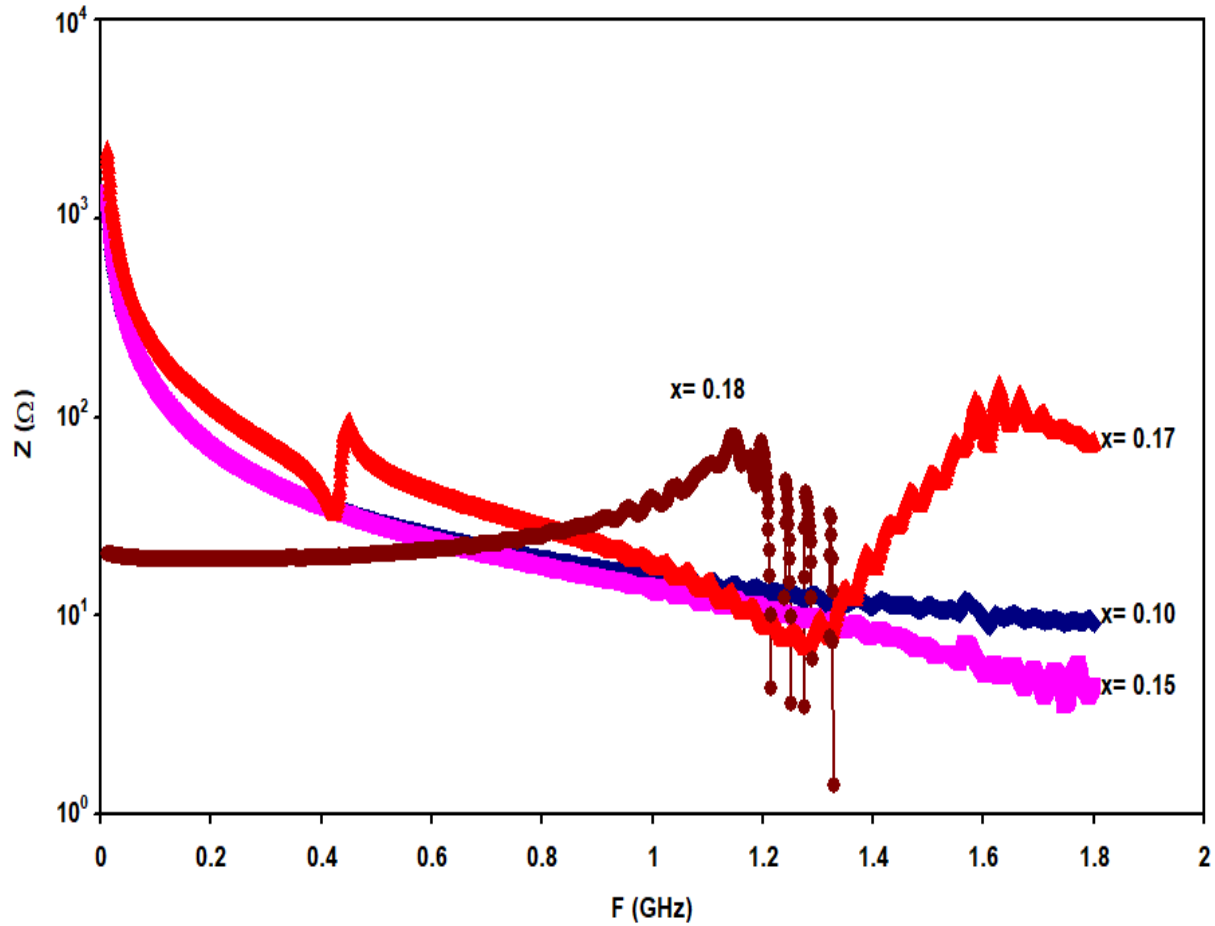


Fig.4.4.3: The Impedance of W-BZN as a function of frequency.

The reflection coefficient is a parameter that describes how much electromagnetic wave is reflected by an impedance discontinuity in the transmission medium. Fig.4.4.4 shows the reflection coefficient (ρ) as a function of frequency. The reflection coefficient of the content of $x = 0.10$ and $x = 0.15$ decreases slowly in the range of 0.01-0.3 GHz then it remains constant in all the studied range. At $x = 0.17$ the reflection coefficient exhibit two minimum values at frequencies of 0.43 GHz and 1.53 GHz. The normal mode of the reflection coefficient equals 1 or zero. In order to transfer data from the source to the device, it must be matched which means

no wave can propagate in this case ($\rho=0$). The nearest point exists for the content of $x=0.17$ at 1.53 GHz. The lower value of ρ , lead to better match between the source and device[37]. In addition, the reflection coefficient for W-content of $x=0.18$ sharply decreases from 0.93 at the frequency of 1.75 GHz to 0.71 at the frequency of 1.79 GHz.

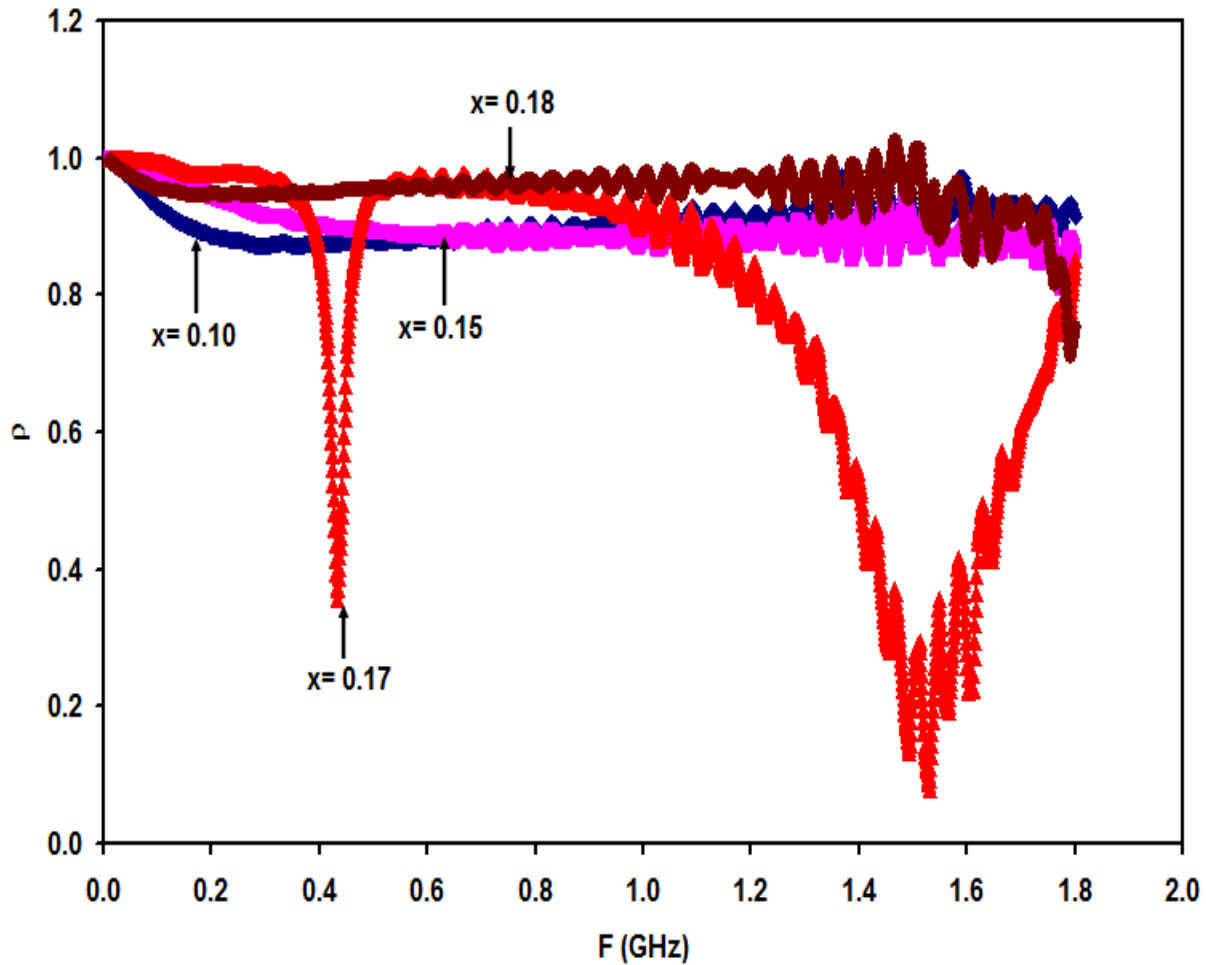


Fig.4.4.4: The Reflection coefficient of W-BZN as a function of frequency.

To detect information about the trapped wave quality, the return loss spectra are calculated and presented in Fig.4.4.5. The higher the return loss (L_r) value (ideally should equal 20 dB), the more qualitative the wave trap [38]. The illustrated spectra of L_r indicate that the addition of tungsten for the doping ratio $x= 0.17$ in BZN makes it ideal for wave trapping at notch frequency of 1.53 GHz, but the content of $x= 0.10$, 0.15 and 0.18 failed to reach the same quality.

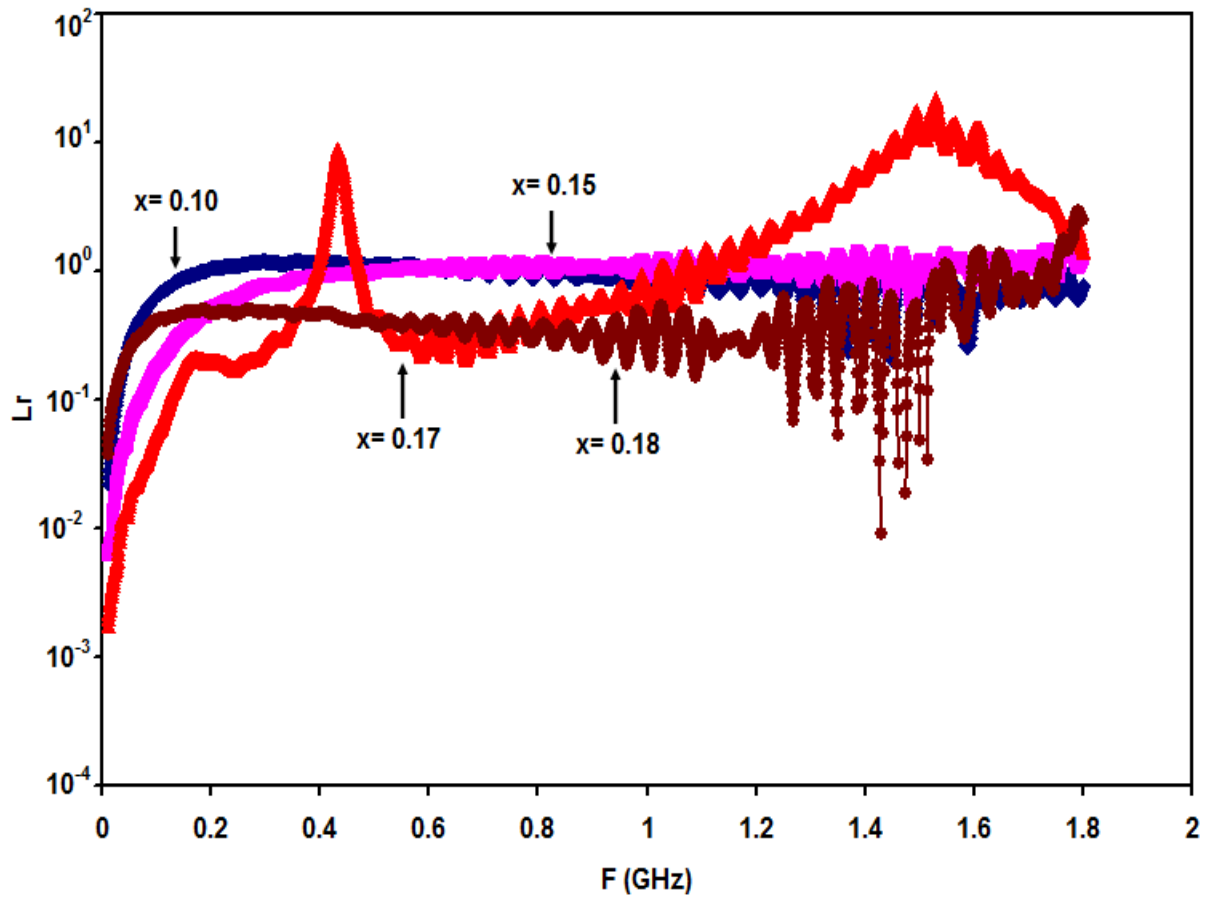


Fig.4.4.5: The Return loss of W-BZN as a function of frequency.

Fig.4.4.6. shows Voltage Standing Wave Ratio (VSWR) as a function of frequency. VSWR is a function of the reflection coefficient, which describes the power reflected from samples. The VSWR is always real and positive number for antennas. The smaller the VSWR is, the better delivered the power. The minimum VSWR is 1. It is clear that this property appears at the content of $x=0.17$ at the frequency at about 1.5 GHz.

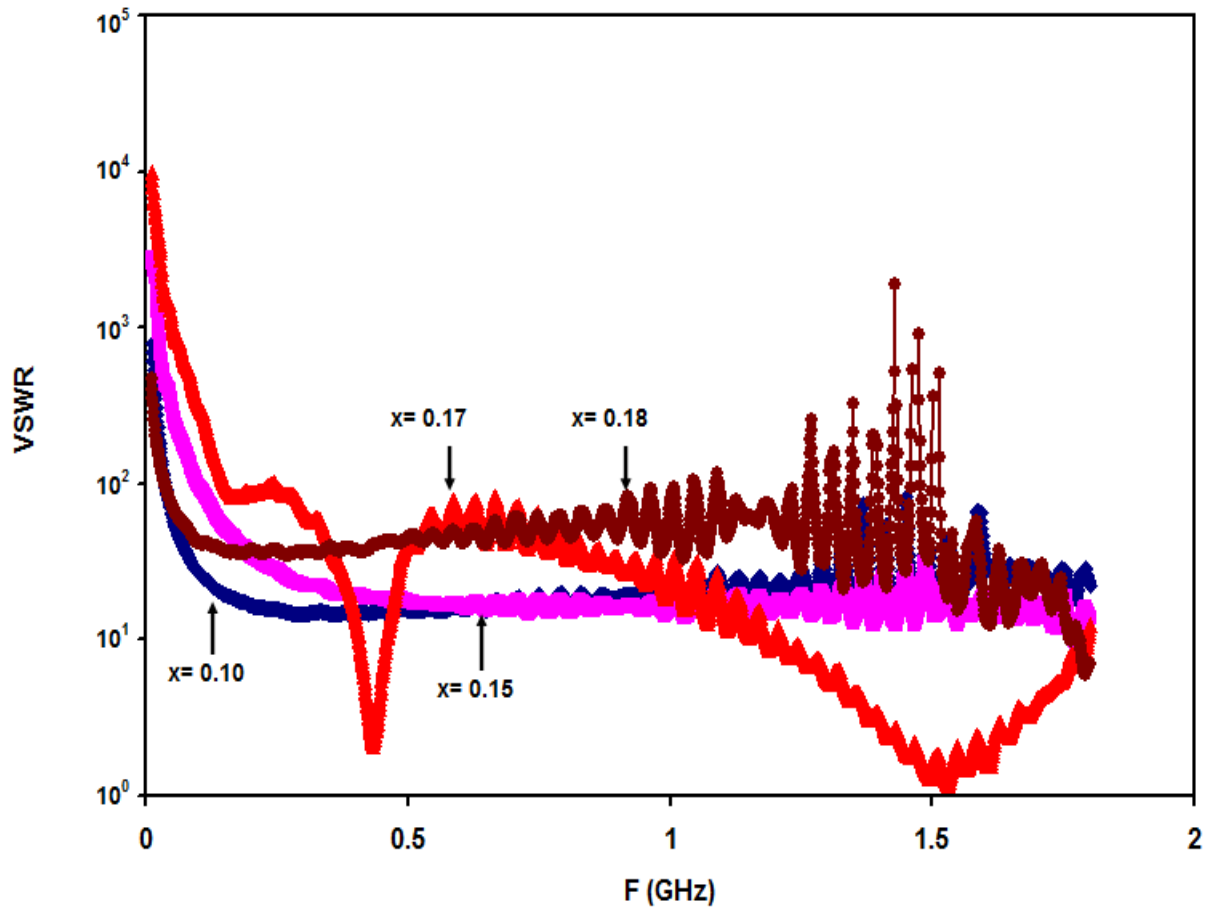


Fig.4.4.6: The VSWR of W-BZN as a function of frequency.

4.5: Electrical properties for $\text{Bi}_{1.5}\text{Zn}_{0.92}\text{Nb}_{1.5-6x/5}\text{W}_x\text{O}_{6.92}$:

In this part, we explore the effect of the tungsten doping on the electrical performance of the BZN. The temperature dependent electrical resistivity is measured for the samples. The electrical resistivity for each of pyrochlores is recorded in the temperature range of 298-478 K. Fig.4.5.1 shows the electrical resistivity as a function of temperature (T). The electrical resistivity of W-BZN displays two regions of variation 298-412 K and 412-478 K. In the region of 298-412 K, the electrical resistivity remains constant. The electrical resistivity sharply decreases with increasing temperature from 412 K to 478 K. The electrical resistivity decreases with increasing temperature. The decrease in the values of the electrical resistivity with increasing temperature can be regarded as transition temperature from insulator to semiconductor type of materials. Similar behavior is also observed for $\text{Bi}_{1.5}\text{Zn}_{0.92}\text{Nb}_{1.5}\text{O}_{6.92}$ (BZN) doped with lanthanum (La) [6]. In addition, the resistivity, approximately, decreases with increasing the tungsten doping the ratio at room temperature due to the increase in the free carrier concentration. It exhibits values of 66.69×10^6 , 17.24×10^6 , 24.62×10^6 , and 3.29×10^6 ($\Omega\cdot\text{cm}$) as the tungsten content increases from 0.10, 0.15, 0.17 and 0.18 respectively.

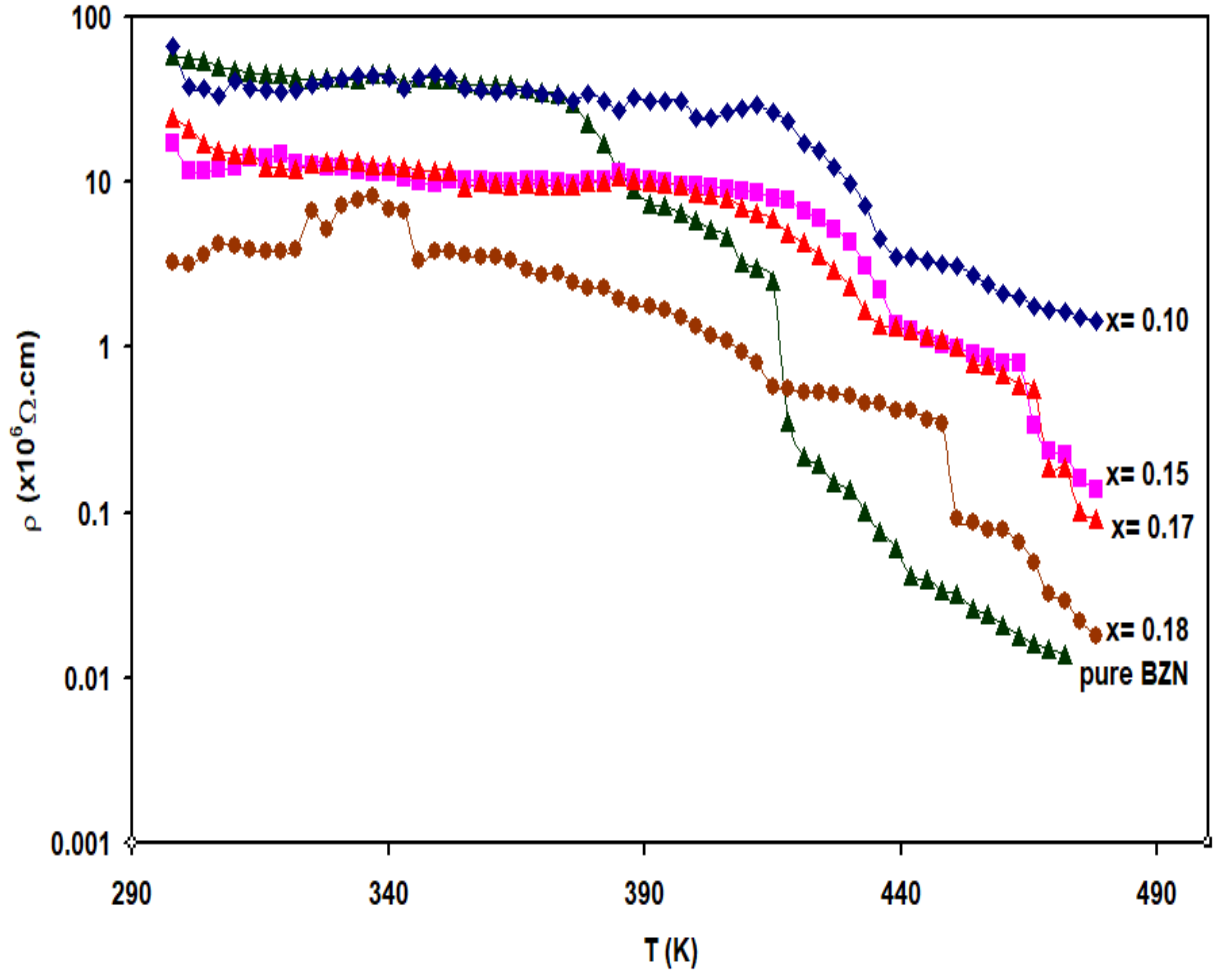


Fig.4.5.1: Variation of electrical resistivity of the W-BZN with temperature.

The plot of $\ln(\rho)$ as function of $1000/T$ is shown in Fig. 4.5.2 and the activation energies (E_a) for W-BZN is shown in table 4.5.1. This shows the activation energies of 1.22, 0.83, 0.81 and 0.21 eV for the 0.10, 0.15, 0.17 and 0.18 W-doped samples, respectively, and the activation energy of the pure BZN is 1.29 eV. It indicates the extrinsic type of conduction because the value of activation energy is less than half the energy band gap (E_g of BZN is equal 3.3 eV).

Thermal energy works to help the electron to overcome energy barriers between the grains and those created in two ways either by tungsten impurities and the defects or dislocation density produced during the sample preparation process [6].

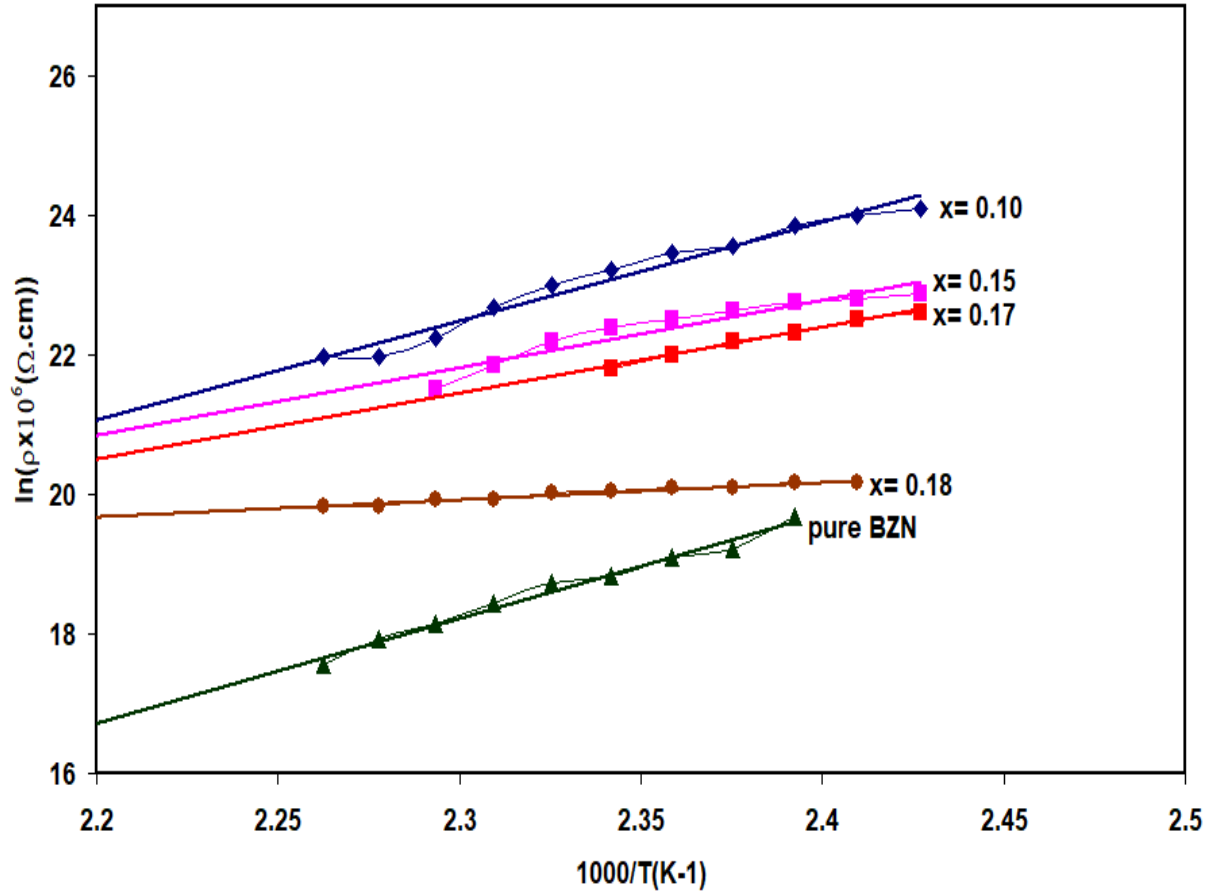


Fig.4.5.2: The $\ln(\rho)$ - $1000/T^{-1}$ dependence.

Table 4.5.1: The activation energy of W-BZN from $x=0.10$ to $x=0.18$.

W content	pure	0.10	0.15	0.17	0.18
E_a (eV)	1.29	1.22	0.83	0.81	0.21

4.6: Optical properties $\text{Bi}_{1.5}\text{Zn}_{0.92}\text{Nb}_{1.5-6x/5}\text{W}_x\text{O}_{6.92}$:

In this part, we study the effect of tungsten doping on the optical properties of BZN. The transmittance, reflectance, absorption coefficients and energy band gaps are considered.

As shown in Fig.4.6.1 the transmittance spectra have two distinct incremental trends below and above 298 nm for pure BZN ceramics. The transmittance spectra in all samples sharply increase with increasing incident light wavelength in the range of 216-300 nm. Above 300 nm, transmittance spectra saturate at constant value. This behavior may have occurred due to the changes in the atomic bonds that are associated with W atom injection into the BZN structure. The BZN doped with samarium (Sm) has the same behavior of the transmittivity [39]. The transmittance spectra red shifts as the doping content increases. In addition, the transmittivity decrease as the doping content increases. Comparing the transmittance of samples doped with $x=0.15$ and $x=0.17$ which exhibit the same powder thickness it is possible to see that the transmittivity increases with decreasing doping content.

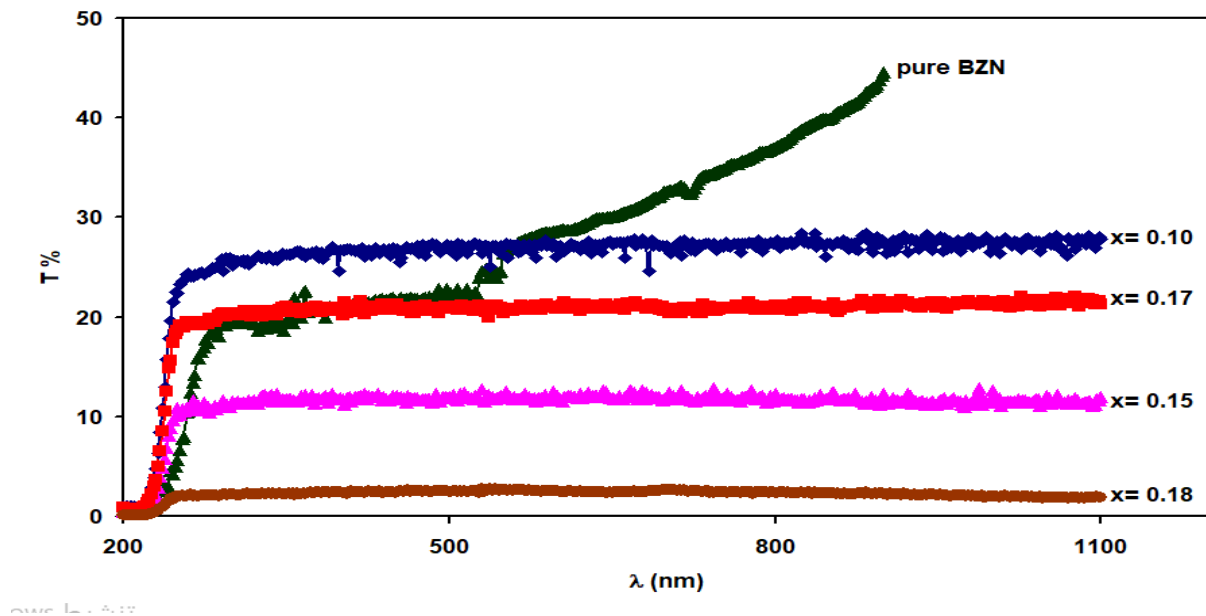


Fig.4.6.1: The transmittance of $\text{Bi}_{1.5}\text{Zn}_{0.92}\text{Nb}_{1.5-6x/5}\text{W}_x\text{O}_{6.92}$ solid solutions.

Fig.4.6.2 presents the reflectance spectra of W-BZN for two regions of variation 200-440 nm and 440-820 nm. For the incident light wavelengths in the region of 820-1100 nm, the reflectance increases with increasing incident wavelengths in all W-BZN. The values of reflectance are very low due to the surface roughness. The pyrochlore ceramics are observed to exhibit accumulated grains of large sizes. These grains cause diffuse reflectance rather than specular which make reflectivity measurements hardly possible. The reflectance decreases with increasing doping ratio. It exhibits values of 0.640, 0.551, and 0.431% for $x=0.10$, 0.15 and 0.18, respectively, at $\lambda=1100$ nm. At $x=0.17$, reflectance has the maximum of 0.660% at $\lambda=1100$ nm. The reflectance of the content of $x=0.17$ is larger than that of $x=0.15$. The reflectance for the pure BZN has the largest value which is equal 1.38 % for $\lambda=1100$ nm.

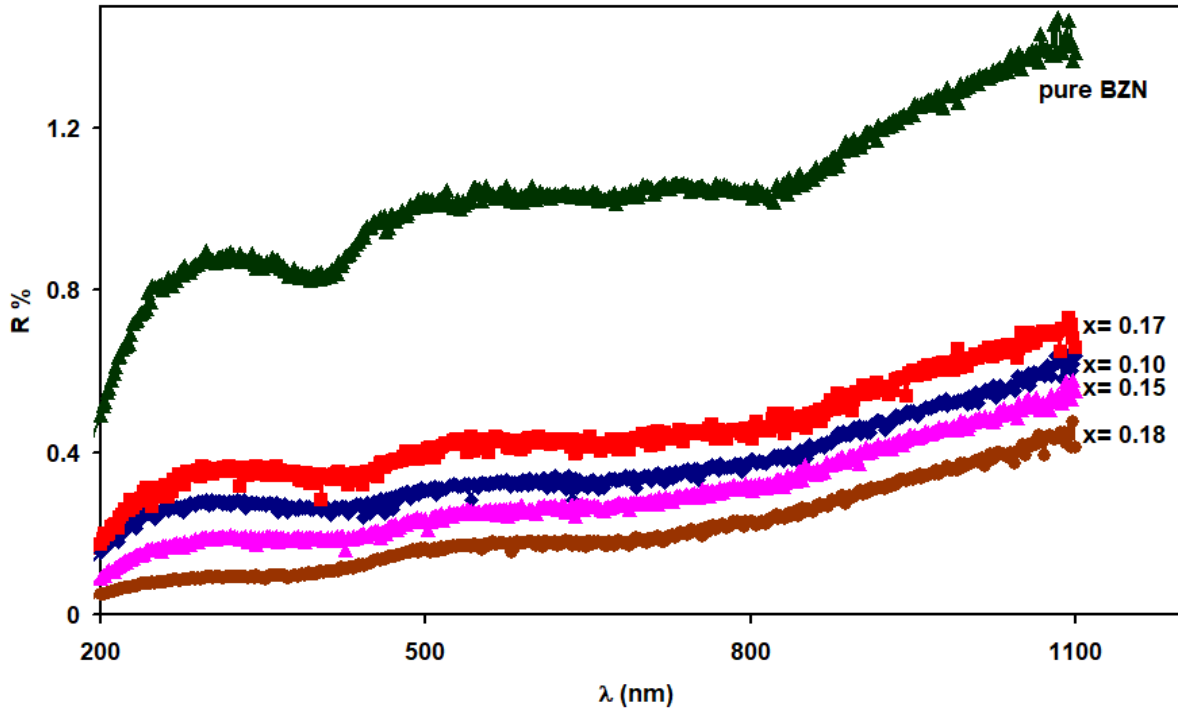


Fig.4.6.2: Reflectance of $\text{Bi}_{1.5}\text{Zn}_{0.92}\text{Nb}_{1.5-6x/5}\text{W}_x\text{O}_{6.92}$ solid solutions.

To reveal complete information about the optical band gap of the doped pyrochlore, the absorption coefficient (α) of W-BZN are calculated from the measured transmittance and reflectance at normal incidence using the relation

$$T = (1 - R)e^{-\alpha d} \quad (4.1)$$

Where R is the reflectance, T is the transmittance and d is thickness.

For the pure BZN, the absorption coefficient increases for all study values. All doped samples have the same behavior. α has three regions of variation, the constant absorption coefficient in the region of 1.12-5.01eV, the sharp increase with increasing photon energy in the region of 5.01-5.80 eV, and absorption saturation in the region of 5.80-6.21 eV. α increases with increasing doping content, this is attributed to the increasing of number of charge carriers, hence, increase the absorbance and absorption coefficient [40]. This behavior also observed in the polyvinyl alcohol and carboxyl methyl cellulose (PVA–CMC) blend doped by Niobium carbide nanoparticles. Namely, at E= 5.8 eV for example, α exhibits values of 1.45, 3.02, 2.72, 3.52x10⁴ cm⁻¹, as the doping content increases from 0.10, 0.15, 0.17 and reached 0.18, respectively, for pure BZN α equal 2.75 x10⁴ cm⁻¹.

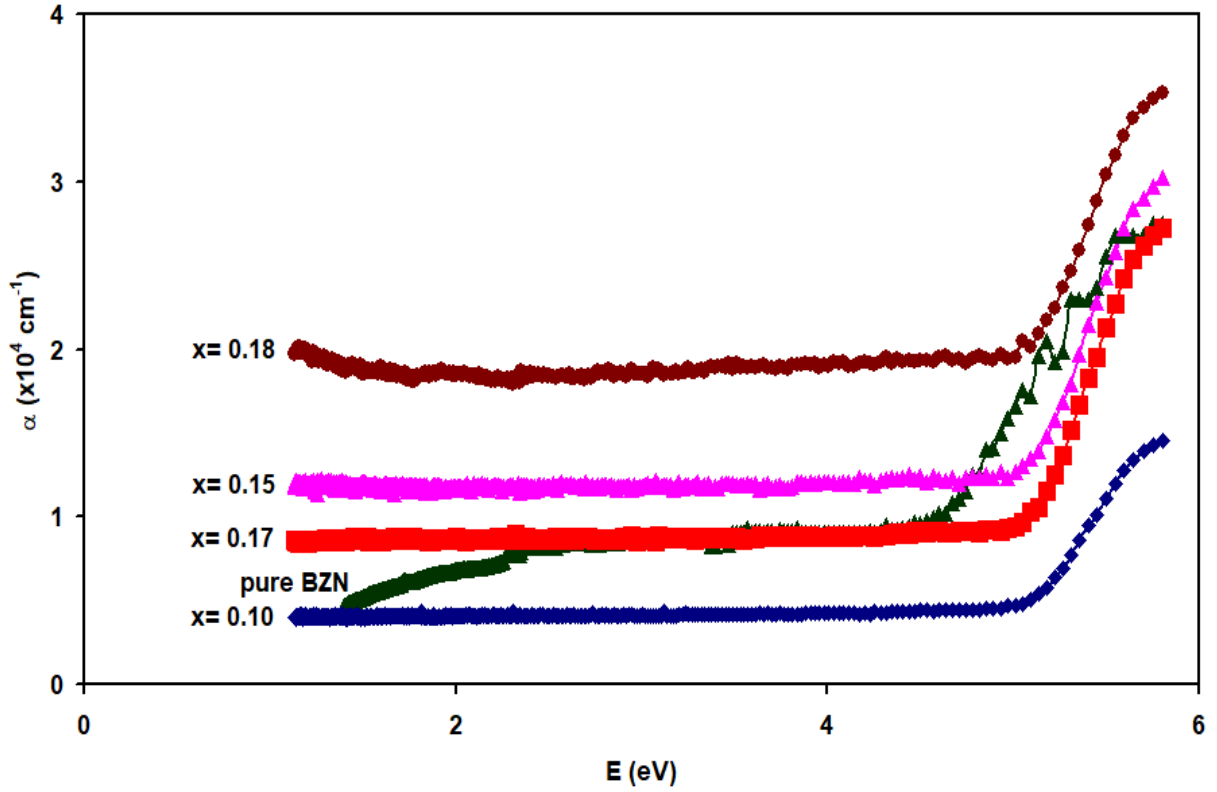


Fig.4.6.3: Absorption coefficient of $\text{Bi}_{1.5}\text{Zn}_{0.92}\text{Nb}_{1.5-6x/5}\text{W}_x\text{O}_{6.92}$ ceramics.

To reveal detailed information about the energy band gap, α - E dependences are calculated using Tauc's equation (3.6)

$$(\alpha E)^{\frac{1}{p}} = B(E - E_g) \quad (4.2)$$

Where B is a constant that depends on the transition probability and p is an index that characterizes the optical absorption process and is theoretically equal to 2, 1/2, 3 or 3/2 for indirect allowed, direct allowed, indirect forbidden and direct forbidden transitions, respectively.

The usual method for determining the value of the band gap, E_g , at fixed temperature, involves

plotting a graph of $(\alpha E)^{1/p}$ versus photon energy, E , in accordance to Eqn. (3.6). If an appropriate value of p is used to obtain linear plot, the value of E_g will be given by the intercept on the E -axis. Applying this relation for the samples under investigation, the $(\alpha E)^{1/2}$, $(\alpha E)^2$, $(\alpha E)^{1/3}$ and $(\alpha E)^{2/3}$ variation as function of E are plotted. The best fitting of the Tuac's equation in the sharp absorption region which is shown in Fig.4.6.4 and Fig.4.6.5 are observed for $1/p=2$ and $1/2$, which are related to direct allowed and indirect allowed transition, respectively. The direct band gap values were determined as $E_g= 5.17, 5.12, 5.16$, and 5.0 eV at 300 K for x values of $0.10, 0.15, 0.17$ and 0.18 , respectively, in the W-BZN ceramics. For the pure BZN the energy gap is 4.76 eV.

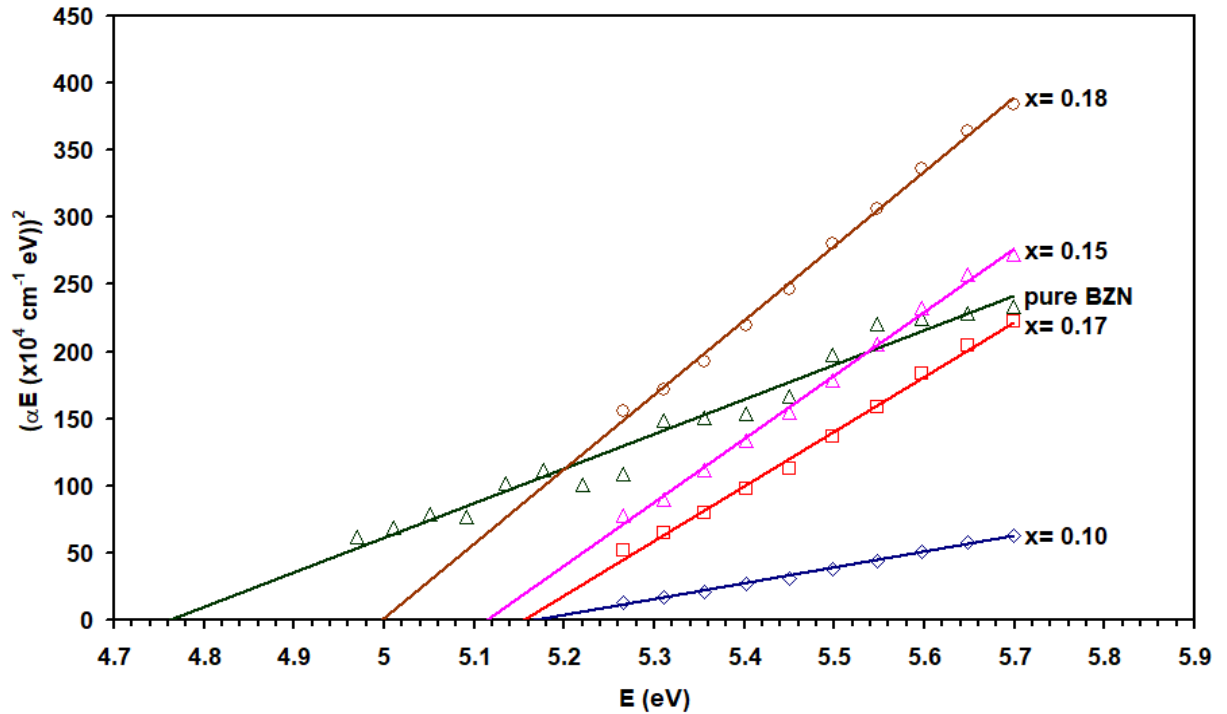


Fig.4.6.4: $(\alpha E)^2$ versus E for W doped BZN pyrochlore ceramics.

Fig.4.6.5 displays the indirect band gaps $E_g = 4.36, 4.10, 4.30$ and 3.61 eV at 300 K for 0.10, 0.15, 0.17 and 0.18 tungsten doped BZN respectively and the energy gap of pure BZN is 3.42 eV. The tungsten causes p-type doping so the materials give holes. Thus the valance band needs more electrons, which increases the band gap [41]. At $x = 0.10$ the dissolved tungsten amount is insufficient to cause a change in the substance. The band gap increases with increasing doping ratio from $x = 0.15$ to $x = 0.17$.

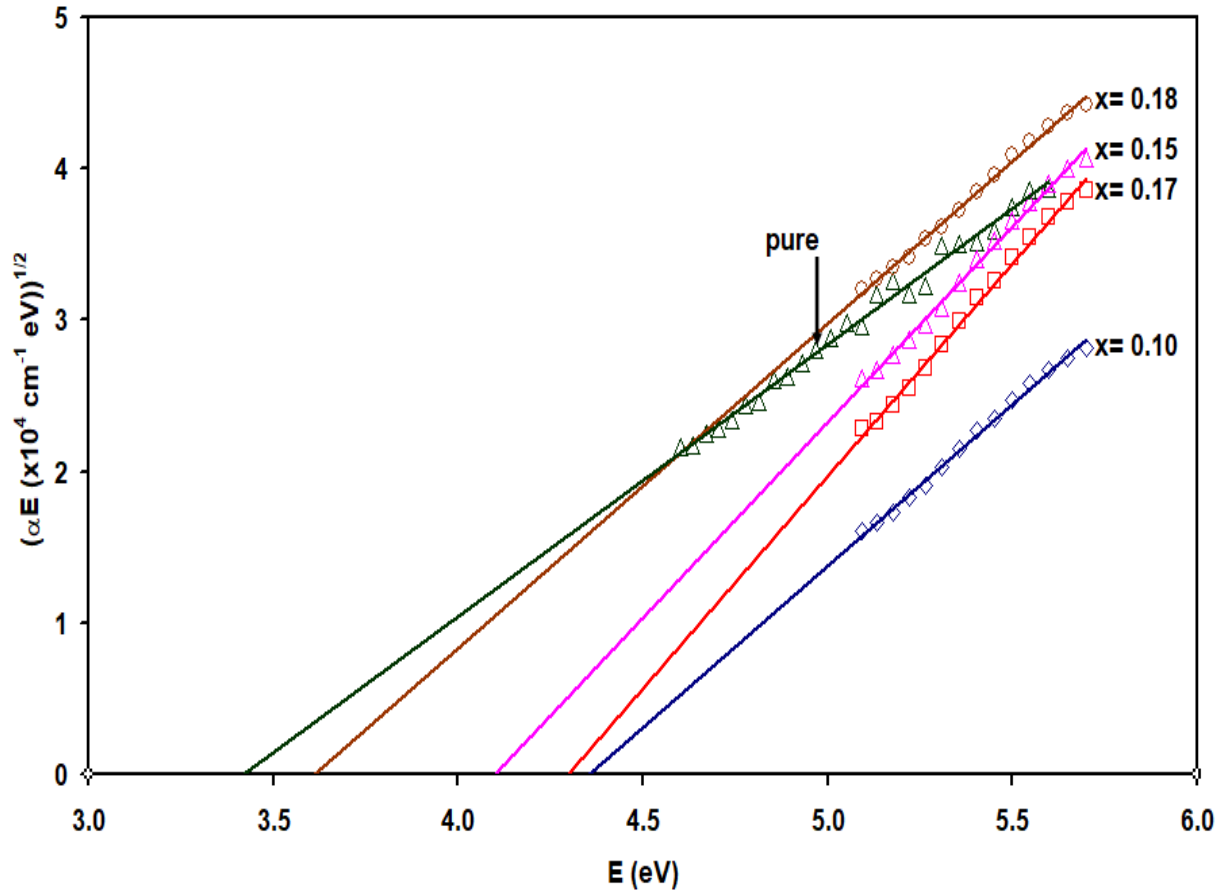


Fig.4.6.5: $(\alpha E)^{1/2}$ versus E for W doped BZN.

Conclusions:

In this thesis, we have studied the tungsten doping effects on the structural, optical and electrical properties of the $\text{Bi}_{1.5}\text{Zn}_{0.92}\text{Nb}_{1.5}\text{O}_{6.92}$ (BZN) pyrochlore ceramics. The doping of W into BZN in accordance with the empirical formula $\text{Bi}_{1.5}\text{Zn}_{0.92}\text{Nb}_{1.5-6x/5}\text{W}_x\text{O}_{6.92}$ has shown that the over solubility limit is reached at $x= 0.18$. For this doping content, three different minor phases appeared. The structural analysis which are investigated as function of doping and temperature has shown that the pyrochlore ceramics exhibit cubic structure with lattice parameter that decreases with increasing doping content below the solubility limit. This effect caused an increase in the grain size and decrease in the strain and defect density. Electrically, the doping resulted in shallower impurity level causing lower values of electrical resistivity. The values of the activation energy are less than the band gap by taking the $\ln\rho$ as a function of reciprocal temperature. In addition, we discussed the problem of studied impedance spectroscopy and studied all electrical properties (impedance, conductance and reactance) for each sample in the range of 0.01-1.8 GHz. The minimum value of the impedance is exhibit at the frequency of 1.32 GHz. The impedance spectra scopy analysis below the solubility limit has shown that the sample doped with W-content of 0.17 is appropriate for use as band stop filters of at least two channels. This property makes the BZN ceramics attractive for use as microwave cavities. Optically, the W- doping force the material to exhibit large value of energy band gap. Both of the direct and indirect energy band gaps decreases with increasing tungsten content. On the other hand, the temperature dependent studies on the structural properties of the pyrochlore have shown that the material could exhibit enhanced crystallinity upon heating. The grain size increases and both of the strain and defect density decreases with increasing temperature. We believe that with this

doping agent. The BZN pyrochlore ceramics are attractive for use in microwave technology that needs high temperature performances.

References:

- [1] WANG, Xu, et al. Microwave dielectric properties and applications of Ba (Zn 1/3 Nb 2/3) O 3–Ca (Zn 1/3 Nb 2/3) O 3 composite ceramics by one-step synthesis method. *Journal of Materials Science: Materials in Electronics*, 2014, 25.11: 4720-4724.
- [2] AL GARNI, S. E.; QASRAWI, A. F.; MERGEN, A. Physical properties of the Bi_{1.5}Zn_{0.92}–2xHfxNb_{1.5}O_{6.92} solid solutions. *Ceramics International*, 2016, 42.2: 3372-3379.
- [3] KHUSAYFAN, Najla M.; KHANFAR, Hazem K. Properties of Hf-Doped Bi_{1.5}Zn_{0.92}Nb_{1.5}O_{6.92} Ceramic Varicaps. *IEEE Transactions on Electron Devices*, 2016, 63.1: 471-475.
- [4] AHMED, Aftab; GOLDTHORPE, Irene A.; KHANDANI, Amir K. Electrically tunable materials for microwave applications. *Applied physics reviews*, 2015, 2.1: 011302.
- [5] YANG, Xinye, et al. Two-step sintering: An approach to prepare Ba (Zn_{1/3}Nb_{2/3}) O₃ ceramics with high degree of cation ordering. *Journal of Alloys and Compounds*, 2017, 723: 930-935.
- [6] QASRAWI, A. F., et al. Mechanical and electrical properties of Bi_{1.5-x}La_xZn_{0.92}Nb_{1.5}O_{6.92} pyrochlore ceramics. *Journal of Electroceramics*, 2016, 37.1-4: 8-14.
- [7] YONG, Peng, et al. Dielectric properties of BZN ceramics doped with Ca²⁺ in A/B-sites. *Ceramics International*, 2017, 43: S228-S231.
- [8] LUO, Weijia, et al. Crystal structure and dielectric properties of Mn-substituted Bi_{1.5}Zn_{1.0}Nb_{1.5}O₇ pyrochlore ceramics as temperature stable LTCC material. *Journal of Materials Science: Materials in Electronics*, 2017, 28.7: 5623-5627.
- [9] JIN, Biao, et al. Sintering behavior and dielectric properties of BZN ceramic powders coated by CuSO₄. *Journal of Ceramic Processing Research*, 2016, 17.7: 712-716.

- [10] WANG, Zhao, et al. Structural and dielectric properties of calcium doped bismuth zinc niobate thin films prepared by pulsed laser deposition at room temperature. *Ceramics International*, 2015, 41: S308-S313.
- [11] Qasrawi, A. F., & Mergen, A. (2013). Effect of yttrium solubility on the structural and optical properties of $\text{Bi}_{1.5-x}\text{Y}_x\text{Zn}_{0.92}\text{Nb}_{1.5}\text{O}_{6.92}$ pyrochlore ceramics. *Ceramics International*, 39(8), 8687-8692.
- [12] Qasrawi, A. F., Nazzal, E. M., & Mergen, A. (2012). Structural, optical, electrical and dielectric properties of $\text{Bi}_{1.5}\text{Zn}_{0.92}\text{Nb}_{1.5-x}\text{Ni}_x\text{O}_{6.92-3x/2}$ solid solution. *Advances in Applied Ceramics*, 111(3), 165-170.
- [13] Mergen, A., Özyoldaş, O., & Küçük, İ. (2012). Production and properties of In and Ir doped $\text{Bi}_{1.5}\text{Zn}_{0.92}\text{Nb}_{1.5}\text{O}_{6.92}$ pyrochlores. *Journal of the European Ceramic Society*, 32(9), 2019-2023.
- [14] Cann, David P., Clive A. Randall, and Thomas R. Shrout. "Investigation of the dielectric properties of bismuth pyrochlores." *Solid state communications* 100, no. 7 (1996): 529-534.
- [15] Arenas, D. J., L. V. Gasparov, Wei Qiu, J. C. Nino, Charles H. Patterson, and D. B. Tanner. "Raman study of phonon modes in bismuth pyrochlores." *Physical Review B* 82, no. 21 (2010): 214302
- [16] Suryanarayana.C & Grant Norton.M. (1998) X-Ray Diffraction: A practical Approach, 1-14.
- [17] Mani Naidu.s.(2011) Engineering Physics-I: For WBUT, 6-6.
- [18] <http://hyperphysics.phy-astr.gsu.edu/hbase/quantum/bragg.html>
- [19] Bindu, P., & Thomas, S. (2014). Estimation of lattice strain in ZnO nanoparticles: X-ray peak profile analysis. *Journal of Theoretical and Applied Physics*, 8(4), 123-134

- [20] M. Abdullah, Derivation of Scherrer Relation Using an Approach in Basic Physics Course, *Jurnal Nanosains & Nanoteknologi*, 1, no. 1, (2008).
- [21] Bhargava.A.K & Sharma.C.P.(2014)*Mechanical Behaviour and Testing of Materials*, 57.
- [22] SKORUPSKA, Katarzyna. Optical properties of semiconductors. *Lecture notes*. Available: http://www.uwyo.edu/cpac/_files/docs/kasia_lectures/3-opticalproperties.pdf. [Accessed: 15-Feb-2016], 2014.
- [23] Bakshi, U. A., & Bakshi, A. V. (2009). *Network analysis*. Technical Publications.
- [24] AILLERIE, M. (2012). Experimental Measurement of Electric Conductivity and Activation Energy in Congruent Lithium Niobate Crystal.
- [25] Besser.L. & Gilmore. R. (2003) *Practical RF Circuit Design for modern Wireless Systems: Passive Circuits and Systems*, 63.
- [26] Pankove, Jacques I. *Optical processes in semiconductors*. Courier Corporation, 2012, *Solar Energy for Fuels* edited by Harun Tüysüz, Candace K. Chan.
- [27] <http://pd.chem.ucl.ac.uk/pdnn/inst1/optics1.htm>
- [28] HREŠČAK, Jitka, et al. Donor doping of $K_{0.5}Na_{0.5}NbO_3$ ceramics with strontium and its implications to grain size, phase composition and crystal structure. *Journal of the European Ceramic Society*, 2017, 37.5: 2073-2082.
- [29] MUSTAFA, Ghulam M., et al. Tunable structural and electrical impedance properties of pyrochlores based Nd doped lanthanum zirconate nanoparticles for capacitive applications. *Ceramics International*, 2018, 44.2: 2170-2177.
- [30] Lu, Da-Yong, Tateaki Ogata, Hidero Unuma, Xue-Cui Li, Na-Na Li, and Xiu-Yun Sun. "Self-compensation characteristics of Eu ions in $BaTiO_3$." *Solid State Ionics* 201, no. 1 (2011): 6-10.

- [31] Hardy, An, S. Van Elshocht, C. Adelmann, T. Conard, A. Franquet, Olivier Douhéret, Ilse Haeldermans et al. "Aqueous solution–gel preparation of ultrathin ZrO₂ films for gate dielectric application." *Thin Solid Films* 516, no. 23 (2008): 8343-8351.
- [32] Salarizadeh, Parisa, Mehran Javanbakht, and Saeed Pourmahdian. "Fabrication and physico-chemical properties of iron titanate nanoparticles based sulfonated poly (ether ether ketone) membrane for proton exchange membrane fuel cell application." *Solid State Ionics* 281 (2015): 12-20.
- [33] QASRAWI, A. F.; JARADAT, Haneen NM; MERGEN, A. Cobalt Doping Effects on the Mechanical and Electrical Parameters of Bi₁₋₅Zn_{0.92}Nb_{1.5}O_{6.92} Solid Solution. *Transactions of the Indian Ceramic Society*, 2014, 73.3: 233-238.
- [34] OMAR, A.; QASRAWI, A. F.; GASANLY, N. M. Temperature effects on the structural and optical properties of the TlInSe₂xS₂ (1– x) mixed crystals (x= 0.3). *Journal of Alloys and Compounds*, 2017, 724: 98-102.
- [35] Brinker, C. J., & Scherer, G. W. (2013). *Sol-gel science: the physics and chemistry of sol-gel processing*. Academic press.
- [36] Tianxiu, S., Shihua, D., Qian, Z., & Zhuowei, Z. (2013). The effect of MgO on the structure and dielectric properties of α -BZN ceramics. *Ferroelectrics*, 451(1), 62-67.
- [37] QASRAWI, A. F.; ALKAREM, Qotaibah A.; GASANLY, N. M. Temperature-dependent structural transition, electronic properties and impedance spectroscopy analysis of Tl₂InGaS₄ crystals grown by the Bridgman method. *Materials Science in Semiconductor Processing*, 2018, 84: 76-82.

- [38] ABED, Tamara Y.; QASRAWI, A. F.; AL GARNI, S. E. Investigation of the physical properties of the Yb nanosandwiched CdS films. *Journal of Alloys and Compounds*, 2018, 731: 1022-1028.
- [39] QASRAWI, A. F.; MERGEN, A. Dielectric dispersion and energy band gap of $\text{Bi}_{1.5-x}\text{Sm}_x\text{Zn}_{0.92}\text{Nb}_{1.5}\text{O}_{6.92}$ solid solution. *Physica B: Condensed Matter*, 2014, 440: 48-52.
- [40] Hashim, Ahmed, and Qassim Hadi. "Synthesis of novel (polymer blend-ceramics) nanocomposites: structural, optical and electrical properties for humidity sensors." *Journal of Inorganic and Organometallic Polymers and Materials* (2018): 1-8.
- [41] YANG, Yu, et al. Electron affinity of cubic boron nitride terminated with vanadium oxide. *Journal of Applied Physics*, 2015, 118.16: 165310.

Conferences

- ❖ Mays A. Abd Al Ghafoor, A. F.Qasrawi (poster). Temperature dependent deformation in BZN pyrochlore ceramics, Sixth Palestinian Conference on Modern Trends in Mathematics and Physics, Palestine Technical University-Kadoorie -Tulkarm.

- ❖ Mays A. Abd Al Ghafoor, A. F.Qasrawi (Poster). Optical properties of ZnPc. Second Palestinian International Conference on Material Science and Nanotechnology, An-Najah National University- Nablus.

الملخص

في هذه الأطروحة، تم دراسة تأثير تطعيم خزفيات البيروكسل BZN بمادة التنجستون على الخصائص الهيكلية والكهربائية والضوئية. أثناء دراسة الخصائص الهيكلية ل W-BZN ظهر لدينا طور ثانوي جديد عند $x = 0.18$. تم دراسة تأثير درجة الحرارة على ثابت البنية، حجم الحبيبة، كثافة الخلع ودرجة التوجه. بالإضافة الى ذلك، تم دراسة مقدار الممانعة لخزفيات البيروكسل عند درجة حرارة الغرفة في نطاق التردد 1.8-0.01 جيجا هيرتز. من خلال دراسة الخصائص التالية: السعة، الموصلية، معامل الانعكاس، خسارة العائد ونسبة الموجة الدائمة للجهد أثبتنا فعالية BZN في الاتصالات التكنولوجية. درسنا المقاومة الكهربائية بواسطة التيار المستمر في نطاق درجة الحرارة 487-298 كلفن. من خلال الدراسة الضوئية لتأثير تطعيم BZN بمادة التنجستون وجدنا بأن طاقة التنشيط أقل من نصف نطاق فجوة الطاقة بحيث تشير الى الطبيعة التوصيل الخارجية.